Validation and Application of a Coupled Xenon Transport and Reactor Dynamic Model of the Molten Salt Reactor Experiment

Jiaqi Chen[1*] and Caleb S. Brooks[2]

[1]*School of Energy and Power Engineering, University of Shanghai for Science and Technology, Shanghai, 200093, China*

[2]*Department of Nuclear, Plasma, and Radiological Engineering, University of Illinois at Urbana-Champaign, Urbana, IL 61801, USA*

*Jiaqi Chen

School of Energy and Power Engineering

University of Shanghai for Science and Technology

516 Jungong Road

Shanghai, 200093, P.R. China

Tel: +86 156-654-22570

Email: jiaqic@usst.edu.cn

Validation and Application of a Coupled Xenon Transport and Reactor Dynamic Model of the Molten Salt Reactor Experiment

The liquid-fueled molten salt reactors have distinguishing dynamic features compared with solid-fueled reactors, such that conventional system analysis codes are not directly applicable. In this study, a coupled dynamic model of the Molten Salt Reactor Experiment (MSRE) is developed. The coupled model includes the neutronics and single-phase thermal hydraulics modeling of the reactor, and the validated xenon transport modeling from previous studies. The coupled dynamic model is validated against the frequency response and transient response data from the MSRE where good agreement is found. The validated model is then applied to study the influences of xenon and void transport on the dynamic behaviors of the reactor. The plant responses during unique initiating events of off-gas system blockage and loss of circulating void are investigated.

Introduction

The 2016 Paris Climate Accords set the goal of limiting the increase of global temperature 1.5~2 °C higher than pre-industrial levels [1], which calls for rapid action in carbon emission curtailment. Nuclear generation is recognized as a crucial part in achieving the net-zero emission goals [2, 3]. In attempts to overcome the economic issues associated with large conventional nuclear reactors, advanced and small modular reactor technologies are being pursued globally, including molten salt reactors (MSRs) [2, 4]. Molten fluoride salt or chloride salt is used as the primary coolant in MSRs, featuring improved safety and thermal characteristics [5, 6].

In liquid-fueled MSRs, fissile and fertile materials (^{235}U, ^{233}U-^{232}Th, and Pu from spent fuel) are dissolved in the fuel salt and circulate in the primary loop [7-10]. Several types of moderators have been considered for thermal spectrum MSRs, including graphite [11], liquid sodium hydroxide [12], and heavy water [13, 14]. The flowing fuel salt in MSRs enables unique features such as intrinsic safety against core melting, passive reactor shutdown through the frozen valve, online refueling, and online removal of fission products [15]. The online refueling and fission product removal features could enable flexible operation of MSRs, which will be increasingly valuable as the share of intermittent generation increases on the grid [11, 16, 17]. The flexible operation of MSRs is facilitated by the removal of xenon. ^{135}Xe is the major thermal neutron poison produced during reactor operation, while other unstable xenon isotopes (mainly ^{133}Xe and ^{131m}Xe) are important radioactive source terms [18, 19]. Xenon and the relatively insoluble gaseous fission products readily escape from the fuel salt at the salt-gas interfaces. In MSRE, the salt-gas interfaces include the free surface and droplets in the pump bowl as well as the circulating bubbles through the primary loop [11, 20].

For flexible operation of MSRs, efficient and robust control schemes are sought to minimize the engagement of control rods during frequent power variations. Such a control scheme should ideally incorporate the nonlinear feedback effects from temperature, flow, void, and xenon transport in the reactor. However, due to the differences between MSRs and solid-fueled reactors, conventional system analysis codes are not readily applicable to study the coupled effects in MSRs [21-25]. The major problems come from the circulation of delayed neutron precursors (DNPs) for short-term simulation [25] and the behavior of fission products for long-term calculations [26, 27]. For system analysis purposes, the neutron kinetics of MSRs can be described by the modified point kinetics equations[1] (mPKEs) [25, 28, 29]. One could refer to the work by Dulla et al. [30] as well as Wooten and Powers [25] for a rigorous derivation of mPKEs for liquid-fueled reactors. In long-term simulations, the separation of noble gases and noble metals from the fuel salt has to be considered [31].

In earlier studies, the authors developed a coupled xenon transport model to study the xenon behavior and xenon removal system in MSRs using Simulink/MATLAB [11, 32]. The model was validated against the xenon poisoning data from the Molten Salt Reactor Experiment (MSRE) [18].

---

[1] In this work, the term "modified point reactor equations (mPKEs)" is universally used for PKEs different from those for solid-fueled reactors. Formulation of these equations are varied in the literature. Wooten and Powers [25] attempted to categorize different mPKEs, though their classification does not cover all the models existed, for example the classical model by Kerlin et al. [28].

The coupled model has the capabilities to track the transport of isotopes, heat, and momentum in typical MSRs. In addition, neutron kinetics in the reactor is modeled using mPKEs. In the current work, the coupled model is extended and validated against various dynamic testing data from the MSRE [33-35] to show its capability for plant dynamic simulations. Compared with existing dynamics studies, the current model has added capabilities of void transport and xenon transport. This feature is exploited to study the influence of xenon transport, void transport, and decay heat generation on the dynamic characteristics of the MSRE. Furthermore, the plant responses during unique operational events are investigated.

Review of Studies on MSR Dynamic Simulations

As discussed in the previous section, the differences between MSRs and solid-fueled reactors prevent direct applications of existing system analysis codes. Sustained efforts have been made in recent years to extend existing system analysis codes or develop alternative codes to study the plant dynamics of MSRs. Selected studies are reviewed in this section.

Krepel et al. [36, 37] developed the DYN1D-MSR and DYN3D-MSR code to study the dynamics of MSRs. In the DYN1D-MSR code, the multi-group neutron diffusion equations are solved in the core using nodal expansion techniques, while the 1D transport equations of DNPs are solved in the whole primary loop. The thermal hydraulics of the reactor is also modeled. The reactivity data during pump startup and pump coast-down in the MSRE zero-power experiment was used to validate the neutronics prediction [38]. The coupled model is validated against the thermal-convection test in the MSRE [39]. In the DYN3D-MSR code, the 3D neutron flux is

solved using nodal expansion techniques, while the DNPs are still treated using 1D transport equations.

Cammi et al. [40] studied the dynamics of the Molte Salt Breeder Reactor using the multi-physics code COMSOL. The two-group neutron diffusion equations are used for neutronics. The distribution of DNPs inside the core is resolved, while their decay outside of the core is estimated using an exponential function with fixed loop transit time. They subsequently studied the MSRE plant dynamics using mPKEs with 1D and lumped DNP transport equations [41]. In the 1D DNP transport equations, the axial distribution of the DNPs inside the core is calculated with prescribed neutron flux profile, which is then linearly integrated to yield the total DNPs for use in the mPKEs. The MSRE plant responses following reactivity insertion and its power-to-reactivity frequency response are presented. Zanetti et al. [42] coupled the COMSOL multi-physics model to mPKEs solved in Simulink. The mPKEs are used to provide power and DNP sources, while the multi-physics model solves the neutron diffusion equation in the reactor to produce the shape function, which is used to update the weighted mPKEs parameters. Good agreement is found between the simulations and experiments for reactivity insertion transient and power-to-reactivity frequency responses. He et al. [43] developed a 3D thermal-hydraulics model of a graphite-moderated channel-type MSR with mPKEs and 1D DNP transport equations using COMSOL.

Diniz et al. [44] studied the dynamics of a conceptual one-dimensional reactor with the coupled neutron diffusion and mPKEs. The multi-group neutron diffusion code is utilized to update the importance weighted parameters in mPKEs. The results of the coupled and non-coupled simulation are compared with theoretical results. It is found that the coupled simulation can better

capture reactor oscillation resulting from flowrate changes, because changes in the importance profiles of DNPs are captured.

Zhang et al. [29] and Guo et al. [45] studied the dynamics of the MOSART reactor using mPKEs with in-house code. Lumped DNPs transport equations for the in-core volume and out-core volume are solved. The pump startup and pump coast-down transients in the MSRE were used for validation [38]. Subsequently, Zhang et al. [46] developed a spatial kinetics model where the 2D two-group neutron diffusion equations are solved together with DNPs transport equations. The decay of DNPs outside of the core is approximated using an exponential function. The results are compared with standard PKEs and mPKEs using weighted parameters obtained from the 2D neutronics simulation.

Zhuang et al. [47] developed an in-house code MOREL to study the neutronics in the MSRE. The code includes the 3D neutron multi-group diffusion equations with transport equations for DNPs. The decay of DNPs outside of the core is modeled using an exponential decay function. The pump startup and pump coast-down transients in the MSRE were used for validation [38]. Subsequently, the code is extended to study the dynamics of TMSR-LF [48]. Zhou et al. [49] studied the 1D distribution of fission products and the associated radioactivity in the primary loop of TMSR-LF using the in-house code MSRFP.

Richard et al. [50] modified the TRACE system analysis code to include the thermal-physical properties of FLiBe salt. He [51] also modified TRACE to study the dynamics of MSRE. The mPKEs are implemented using the so-called "circuit solver" method. The model is applied to simulate the reactivity insertion transients in the MSRE. It was noted that the "circuit solver" tends

to cause numerical instability. Hanusek and Juan [52] applied TRACE to study the power and temperature distribution in the MSRE, and the mPKEs are included using the method proposed by He [51].

Shi et al. [53] extended the RELAP5/MOD4.0 code to include the mPKEs with reference to the formulation by Guo et al. [45]. The extended code is validated against the pump startup and pump coast-down transients [38] as well as the thermal-convection test in the MSRE [39]. Chen et al. [17] used the modified RELAP5 code to study the load-following characteristics of a conceptual MSR. Li et al. [54] improved the mPKEs modeling in the modified RELAP5 code by including the 1D DNP transport equations, where the DNP distributions inside the core are resolved. It is shown that the improved model could better capture the reactivity change during pump startup and pump coast-down transients in the MSRE [38]. Comparisons are also made with the reactivity insertion tests [34] and the thermal-convection test [39].

The advanced system analysis code SAM by the Argonne National Laboratory is under active development and has been coupled with other codes for MSRs applications [55, 56]. A 2D model of MSRE has been built and the coupled solution capability is demonstrated [57]. In the MSRE model, the neutron transport equations are solved by Griffin, while the transport equations of DNPs, energy, and momentum are solved by SAM. Salko et al. [58] added a gas transport model to SAM, and the drift flux model is used to account for the slip velocity between the phases. Yang et al. [59] coupled the PROTEUS neutronics code with SAM using the MOOSE framework. The results are compared with the pump startup and pump coast-down transients [38] and the thermal-convection test in the MSRE [39].

In addition to in-house codes and traditional system analysis codes, Simulink/MATLAB has been actively used to model MSRs due to its great extensibility and comprehensive built-in libraries. Singh et al. [60-64] utilized Simulink to perform a series of modeling studies on the dynamics of MSRs. The mPKEs used by Kerlin et al. [28] are adapted in the modeling, while the thermal-hydraulics is considered using customized lumped parameter models. The dynamics model is validated against the frequency response and the reactivity insertion data from the MSRE [60]. Pathirana et al. [65, 66] extended the Simulink model to include decay heat generation, and the influence of fuel depletion is considered using a predefined depletion table. Dunkle et al. [67, 68] studied the effect of xenon removal on load-following of the NERTHUS reactor design with the open-loop control scheme. The general plant dynamics of NERTHUS is also studied using the established Simulink model. Price et al. [69-71] used Simulink to study the xenon behavior in MSRs together with the plant dynamics. Huang et al. [75] used Simulink to study the dynamics of a MSR coupled with an air-steam combined cycle.

Modelica-based codes are utilized for similar reasons as Simulink/MATLAB. A Modelica-based library for MSRs, named TRANSFORM, is developed by the Oak Ridge National Laboratory (ORNL) [72]. The library is used by Greenwood et al. [72] to model the Molten Salt Demonstration Reactor. The model includes general thermal hydraulics components of the primary and secondary system. The transport of fission products and DNPs is included using the so-called "trace substance approach." The reactor dynamics is modeled using mPKEs. A simplified model of the off-gas system is also included where the concentrations of fission products through the system are calculated. A code-to-code comparison between Simulink and Modelica modeling of MSRE is made by Pathirana et al. [73]. Fischer and Bures [74] applied Modelica and the

TRANSFORM library to study the dynamics in the MSRE. The core neutronics is modeled using mPKEs, while the axial power distribution is modeled using a predefined profile. The 1D DNPs transport equations are solved, and their contribution to the mPKEs are evaluated using steady state adjunct flux. The model predictions are validated against the pump transient, reactivity insertion, and the frequency response in the MSRE [34, 38].

Description of the Coupled Model of MSRE

In the previous study, the authors [32] developed a Simulink/MATLAB model to study the xenon behavior in the MSRE. Lumped parameter models have been constructed for pipes, heat exchangers, the xenon removal system components, and the reactor core. Conservation equations of void, heat, momentum, and fission products are solved in the coupled model. The reactor dynamics was modeled using mPKEs [28]. In the current study, the forementioned MSRE model is extended and modified in the following ways,

- The secondary loop of MSRE is included to model the plant response.

- The implementation of mPKEs is overhauled. The effect of fuel circulation on delayed neutron generation is approached by explicitly modeling the transport of DNPs.

- Model parameters for ^{233}U fuel are added.

- The decay heat generation across the primary loop is modeled.

- The void reactivity effect is added. The feedback effects are now calculated using nuclear importance weighted parameters.

General Description of the Simulink Model

The general structure of the model is inherited from a previously developed model [32]. The model has been open sourced on GitHub where the exact implementation can be found [76]. In this subsection, a brief introduction is given on the major governing equations, constitutive relations, and the changes made to the previous model. The important system parameters used in the MSRE model are summarized in Table 1. The components included in the current coupled model are shown in Figure 1.
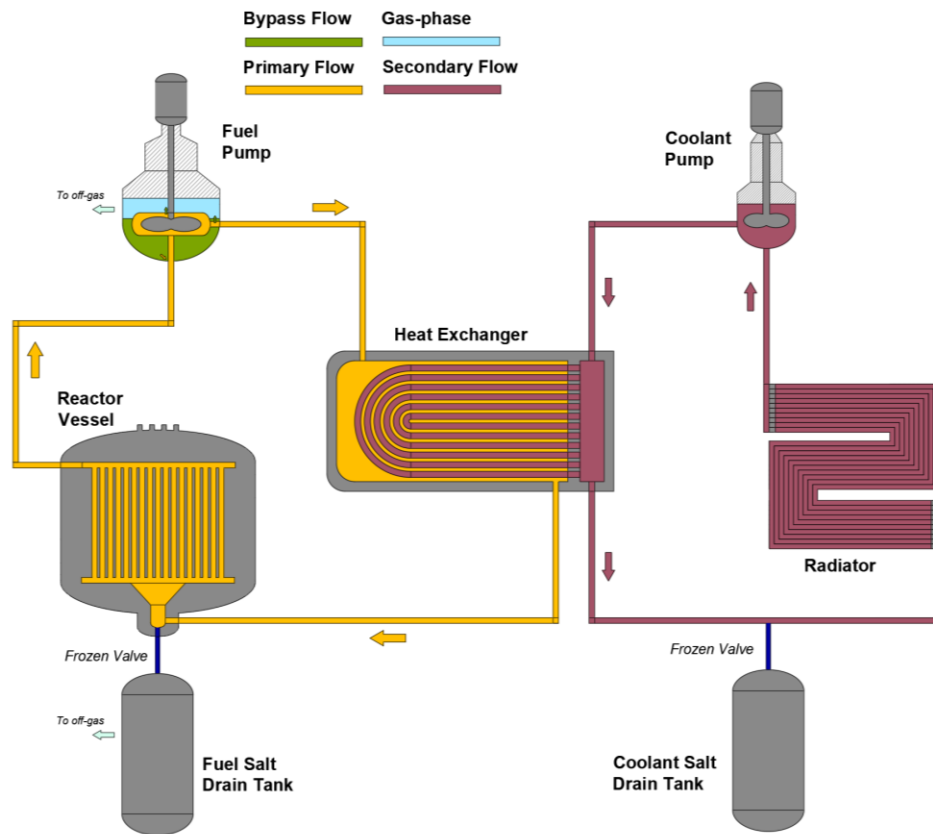

Figure 1. Simplified diagram of the MSRE loop design. All the components and piping are included in the coupled model except for the drain tanks and the frozen valves.

The Simscape toolbox in Simulink is used to provide the building blocks for thermal-hydraulics modeling of the reactor. The descriptions of the Simscape components are readily available in the Simulink/MATLAB documentation. Therefore, detailed discussions of the individual components are omitted. The overall decay heat generation rate is modeled using three decay heat precursor groups with reference to the work by Pathirana et al. [65], and the heat generation in each lumped volume is explicitly calculated.

The transport models for xenon and void fraction were the major efforts in the previous work [32]. The complicated xenon and void transfer processes in the MSRE pump bowl have been modeled using semi-empirical equations. The diffusion of xenon inside the core graphite, the transfer of xenon between the phases and the dissolution of entrained bubbles are described using theoretical and semi-empirical models. The xenon balance equations for a general lumped volume are,

$$\frac{dC_{l,xe}}{dt} = \frac{R_{fission}\gamma_{xe}}{V_{salt}^{core}N_A} + \lambda_I C_I - \lambda_{xe}C_{l,xe} - \phi_{salt}\varsigma_a C_{l,xe}$$
$$-S_{lgr} - S_{lb} + \dot{V}\left(C_{l,xe}^{in} - C_{l,xe}^{out}\right), \tag{1}$$

$$\frac{dC_{b,xe}}{dt} = -\lambda_{xe}C_{b,xe} - \phi_{salt}\varsigma_a C_{b,xe} + S_{lb} - S_{bgr} + \dot{V}\left(C_{b,xe}^{in} - C_{b,xe}^{out}\right), \tag{2}$$

where S_{lgr} is the transfer term between the fuel salt and graphite, S_{lb} is the transfer term between salt and bubbles, S_{bgr} is the transfer term between bubbles and graphite, ς_a is the microscopic absorption cross section of xenon, $R_{fission}$ is the fission rate, ϕ_{salt} is the averaged neutron flux in the fuel salt, and $\dot{V}$ is the volume flowrate of fuel salt. The subscript l means quantities related to the salt, the subscript b stands for quantities related to the gas (bubbles), and the subscript gr is used to represent quantities related to graphite. Outside of the core, the direct fission generation

term, the burnup term, the S_{bgr} term, and the S_{lgr} term are zero, while other terms stay the same. The diffusion of xenon inside the core graphite is calculated by numerically solving the following diffusion equation with burnup and decay terms [84],

$$\frac{dC_{gr,xe}}{dt} = \mathfrak{D}_{gr,xe}\nabla^2 C_{gr,xe} - (\lambda + \phi\varsigma_a)C_{gr,xe}, \tag{3}$$

$$-\varepsilon\mathfrak{D}_{gr,xe}\nabla C_{gr,xe} = J_{xe}, \tag{4}$$

where $C_{gr,xe}$ is the phase averaged xenon concentration, ε is the porosity of graphite, and J_{xe} is the xenon mass flux at the outer boundary of the core graphite. The formation of each term is discussed in the previous publication [32].

The gas/void transport is based on volume conservation and the homogeneous equilibrium model. It is assumed that the gas and the fuel salt move at the same velocity. The solubility of the inert gas bubbles is considered using an algebraic model according to the experimental data taken during the MSRE [20, 32].

Table 1. Key non-neutronics parameters used in the coupled Simulink model of MSRE.

Terms	Specs		Ref.
Salt Properties	[235]U fuel salt composition	[7]LiF-BeF$_2$-ZrF$_4$-UF$_4$ (65%-29.1%-5%-0.9%, 33% Enrichment)	[8]
	[233]U fuel salt composition[a]	[7]LiF-BeF$_2$-ThF$_4$-UF$_4$ (65%-29.1%-5%-0.14%, 91.5% Enrichment)	[77]
	Density[b]	2614.9 - 0.5942T [kg/m^3]	[77, 78]
	Viscosity[b]	1.77E-4 exp(3624/T) [Pa·s]	[79, 80]
	Specific heat capacity	1967.8 [J/kg·K]	[8]
	Thermal conductivity	1.4 [W/m·K]	[80]
Reactor	In-core fuel volume	0.708 [m^3]; 25 [ft^3]	[81]
	Graphite total heat capacity	6.44 [MW· s/K]	[28]

	Plenums, downcomer, and flow distributor volume	0.8552 [m^3]	[81]
	Fission energy in salt	93.4 %	[82]
	Graphite-fuel overall heat transfer coefficient	0.036 [MW/K]	[28]
Primary Pump	Discharge rate	71.6 [L/s]; 1200 [GPM]	[81]
	Bypass rate to pump bowl	4.1 [L/s]; 65 [GPM]	[81]
	Pump bowl volume	0.1359 [m^3]; 4.8 [ft^3]; 60% filled	[31]
	Pump volume	0.0255 [m^3]; 0.9 [ft^3]	[81]
Heat Exchanger[c]	Nominal fuel inlet temperature	935.93 [K]; 1225 [°F]	[81]
	Nominal coolant inlet temperature	824.82 [K]; 1025 [°F]	[81]
	Nominal power	10 [MW]	[81]
	Fuel volume	0.1727 [m^3]; 6.1 [ft^3]	[81]
Primary Piping	Total volume	0.1444 [m^3]; 5.1 [ft^3]	[81]
Secondar Loop	Total coolant volume	1.2672 [m^3]	[33]
	Coolant salt heat capacity	2384.9 [J/kg·K]	[83]
	Coolant salt density	2328.7 - 0.42T [kg/m^3]	[83]
	Flow rate	52.4 [L/s]; 830 GPM	[81]

[a]The concentration of non-uranium elements are slightly changed to balance the change in uranium concentration.
[b]The temperature dependence is taken from data for uranium-free salt, the correlation is linearly scaled to match the reported data for the fuel salt.
[c]The overall heat transfer coefficient is calculated using the nominal values, the mass flowrates, and the material properties with pre-defined heat transfer correlations, see Simscape documentation for more information.

Modified Point Kinetics Equations, the Core Nodes, and the Feedback Effects

In the current model, the implementation of the mPKEs and the calculation of reactivity feedback effects are modified compared with the previous study [32]. These modifications are discussed in this subsection. The neutronics and feedback parameters used for different fuel types are summarized in Table 2.

Table 2. Key neutronics and feedback parameters of MSRE for [233]U and [235]U fuel [28, 85-87].

	Parameters	[233]U Fuel	[235]U Fuel
Point Kinetics	Group Decay Constant, λ_i, [1/s]	[0.0126, 0.0337, 0.139, 0.325, 1.13, 2.5]	[0.0142, 0.0305, 0.111, 0.301, 1.14, 3.014]

Equation Parameters	Group Yield, β_i, $[10^{-4}]$	[2.3, 7.9, 6.7, 7.3, 1.3, 0.9]	[2.23, 14.57, 13.07, 26.28, 7.66, 2.3]
	Neutron Generation Time, Λ, [s]	4×10^{-4}	2.4×10^{-4}
Feedback Parameters	Graphite Temperature, $[\delta k/k \cdot K]$	-5.814×10^{-5}	-6.66×10^{-5}
	Fuel Temperature, $[\delta k/k \cdot K]$	-11.034×10^{-5}	-8.712×10^{-5}
	Core Void, $[\delta k/k]$	-0.45	-0.18

In MSRs, the fuel salt circulates in the primary loop. Thus, the DNPs are transported out of the core. Part of the delayed neutrons are thus lost during the transit time across the primary loop. Moreover, the physical and adjunct neutron flux and DNP concentration profiles are varied under the fuel salt flow. Therefore, a modification is required in the point kinetics equation derived for solid-fueled reactors. The rigorous derivation of mPKEs can be found in Dulla et al. [30, 88] However, such a rigorous approach can only be realized by coupling a neutronics code to the system analysis model, which significantly increases the simulation time. Instead, in the current study, the classical model by Kerlin et al. [28] is selected as the starting point. The model was developed during the MSRE and has been calibrated using the various dynamics testing data obtained from the experiments. Therefore, even though this model is derived without consideration of DNP importances, it turns out to behave quite well when compared with the experiments. The original model proposed by Kerlin et al. [28] is,

$$\frac{dn}{dt} = \frac{\rho - \beta}{\Lambda}n + \sum_{i=1}^{6} \lambda_i C_i + S, \tag{5}$$

$$\frac{dC_i(t)}{dt} = \frac{\beta_i}{\Lambda}n - \lambda_i C_i(t) - \frac{C_i(t)}{\tau_c} + \frac{C_i(t - \tau_l)e^{-\lambda_i \tau_l}}{\tau_c}. \tag{6}$$

The last two terms in Equation 6 correspond to the outflow and inflow of the DNPs at the reactor core. τ_l is the loop transit time outside of the core, and τ_c is the residence time within the core. The assumptions behind these equations are the instant mixing of DNPs inside the core, and the absence of precursor mixing outside of the core.

In the current study, Equation 6 is replaced with a series of lumped conservation equations of DNPs. For each lumped volume, the following equation is solved,

$$\frac{dC_{i,node}(t)}{dt} = \frac{\beta_i}{\Lambda}n - \lambda_i C_i(t) + \frac{\dot{V}C_{i,in}(t)}{V_{node}} - \frac{\dot{V}C_{i,out}(t)}{V_{node}}. \tag{7}$$

If enough lumped equations are included, Equation 7 will converge to Equation 6. This implementation offers three main advantages. First, Equation 7 can be applied to both core node and out-of-core node. It may be used together with a neutronics code to derive the mPKEs using the quasi-static approach similar to Zanetti et al. [42]. Second, by mapping the out-of-core node to each physical component and adding a correction factor to the outflow term, the different mixing behavior inside the corresponding physical component could be accounted for. Lastly, the computer memory requirement is greatly reduced by moving from Equation 6 to Equation 7, which is essential to apply the current coupled model for extended runs and low-flow conditions. In the current implementation, one core node and ten out-core nodes are used without exact mapping between physical components and DNP nodes.

The thermal hydraulic nodal diagram of the reactor is shown in Figure 2, including the upper plenum, the lower plenum, the downcomer, the inlet flow distributor, and four linear core nodes. Axial heat conduction between the graphite nodes and the plenums is included, while the radial

conduction is neglected. The axial power profile and the nuclear importance profile used to calculate feedback effects are taken from the report by Haubenreich et al. [82]
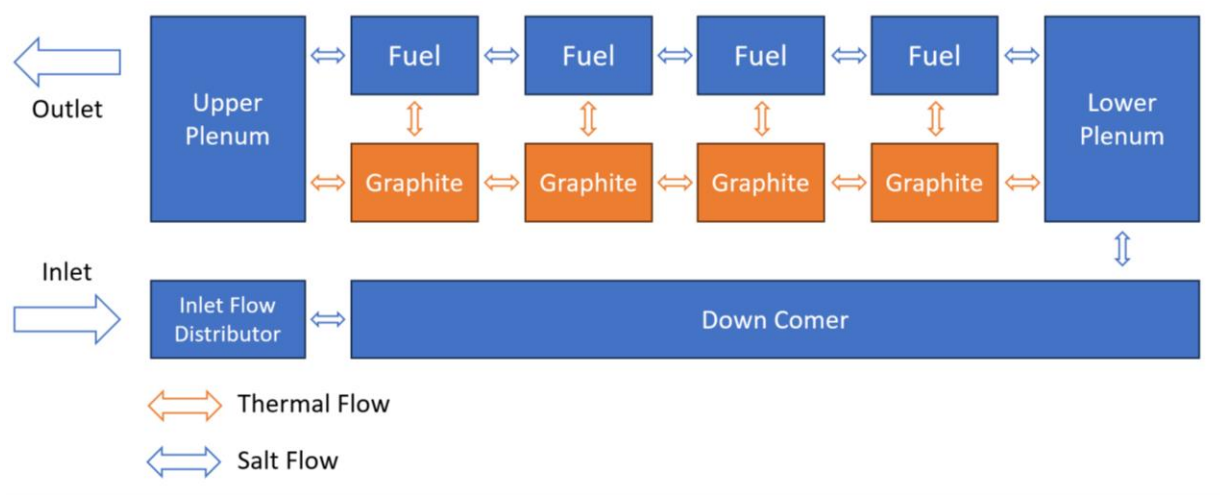

Figure 2. The thermal hydraulic nodal diagram of the MSRE core in the coupled model.

Model Validation against MSRE Dynamics Tests

In this section, the coupled model is validated against various dynamics testing datasets from the MSRE. Both the frequency response and the transient response of the coupled system model are investigated.

Frequency Response

The frequency response of a dynamic system refers to the response of the system to a sinusoidal input signal in the frequency domain. Different frequency responses of a system can be defined based on the selected input signal and output signal. The frequency response can be experimentally measured, which provides valuable information for the controller design and stability analysis [89]. Moreover, a frequency analysis method is useful for the experimental

determination of the reactivity related parameters [38, 89, 90]. During the operation of MSRE, multiple dynamic testing experiments were conducted to obtain the frequency responses of reactor powers to reactivity disturbances [33, 34]. These tests were conducted at different steady-state power levels for both ^{235}U fuel and ^{233}U fuel.

Because the coupled MSRE model is highly nonlinear, the frequency response cannot be obtained from a derived transfer function as in a linearized model. To obtain the frequency response from the coupled MSRE model, numerical experiments are conducted. For each condition, the simulation is first run for three days to reach the steady-state xenon distributions, while the reactor is maintained at critical condition using a PI controller. Then, the PI controller is disabled, the final reactivity insertion is recorded, and the steady-state solution is saved. Using the steady-state solution as a starting point, sinusoidal reactivity signals of different frequencies are introduced into the system, and the simulations are run for a minimum of ten cycles or 1500 seconds. The cross power spectral density between the neutron density signals and the reactivity signals are calculated and then divided by the power spectral density of the reactivity signals. The outcome is a function in the frequency domain due to the finite simulation time. The values at the signal frequencies form the frequency response of the system.

For ^{235}U fuel, simulated frequency responses at three different power levels are presented and compared with experimental data [33], as shown in Figure 3 and Figure 4. Note that different methods were used to obtain the frequency response in the dynamic testing experiments. The results from different methods are not distinguished in the current study, and the spread of data points might be considered as experimental uncertainty. Based on the results, general agreement

is found between the simulation and experiment. The good agreement suggests that the coupled

MSRE model could capture the reactor behaviors under small reactivity disturbances. Cammi et

al. [91], Guerrieri et al. [92] and Henderson and Ragan [93] performed theoretical analyses of the

circulating fuel reactors from a transfer function standpoint using mPKEs. Conclusions and

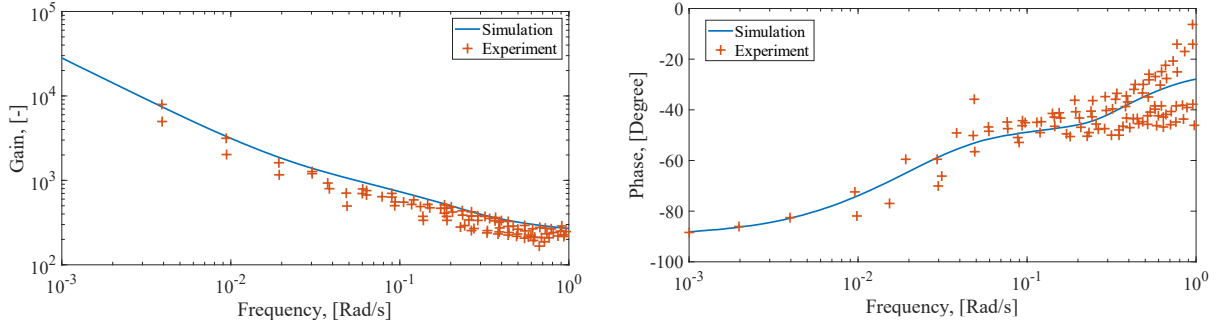equations from these studies are borrowed to aid further discussion on the results.

Figure 3. Comparison of the power-to-reactivity frequency response from simulations and

experiments at zero-power with ^{235}U fuel [35].

In Figure 3, the reactor response at zero-power is presented. This condition is of special

interest because the thermal and poisoning feedback effects are absent. For solid-fueled reactors,

the frequency response at zero-power is predominated by the neutronics models. For MSRs, the

flowrate in the reactor also plays a significant role. It is shown that for low frequencies, the

response of the reactor, $G(jw)$, is approximated by,

$$G(jw) = \frac{\delta n}{n_0 \delta \rho} \approx -\frac{jw_1}{w}, \qquad when\ w \ll 1\ \text{rad/s}, \tag{8}$$

$$w_1 = \frac{\beta}{\Lambda + \sum \beta_i \left(1 + \frac{\tau_l}{\tau_c} \exp(-\tau_l \lambda_i)\right)/\lambda_i}. \tag{9}$$

The result dictates a nearly linear decrease in the log-log plot of the gain, and a frequency lag

starting from -90 degrees, as observed in Figure 3. The agreement between the simulation, theory,

19

and experiment at zero-power gives strong confidence in the validity of the neutronics model adopted in the current study.
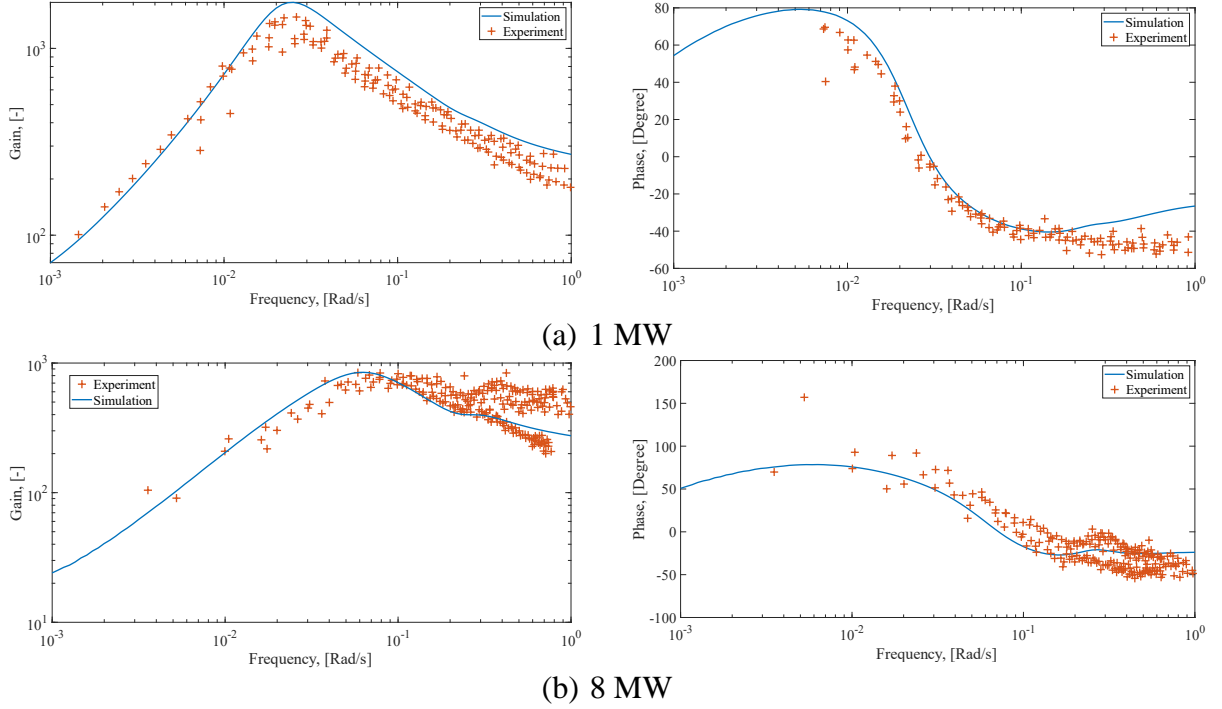

(a) 1 MW

(b) 8 MW

Figure 4. Comparison of the power-to-reactivity frequency response from simulations and experiments at power with ^{235}U fuel [35].

When the reactor is at power, feedback effects from temperature and xenon poisoning take place, and the frequency response of the reactor is complicated. When considering only thermal feedback with an averaged core temperature, the neutron-temperature feedback transfer function may be defined as,

$$H'(jw) = \frac{\delta \rho_t}{\delta n / n_0},$$

(10)

while the closed loop transfer function, $R(jw)$, is derived as,

$$R(jw) = \frac{G(jw)}{1 - G(jw)H'(jw)}. \tag{11}$$

From Equation 11, it is immediately known that when the magnitude of $G(jw)$ is large, $R(jw)$ is dominated by $H'(jw)$, which corresponds to the case at low frequencies. On the other hand, when $G(jw)$ is small, the closed loop function converges to $G(jw)$, as one would expect for high frequency disturbances because the fluctuation ends before the system feedback could react. It can be shown that $H'(jw)$ is proportional to the reactor power, so that higher reactor powers stabilize the reactor. It could also be shown that $H'(jw)/P_0$ is only dependent upon the thermal-hydraulics characteristics. Comparing Figure 4(a) and Figure 4(b), it is observed that the gain of the reactor at higher power is dampened as anticipated. Moreover, the phase difference at lower frequencies is now positive rather than negative as at zero-power, which corresponds to the negative temperature feedback coefficient in $H'(jw)$. The simulation slightly overpredicts the gain at 1MW, but satisfactorily predicts the gain at 8 MW. This reflects the imperfections of the thermal hydraulics modeling employed in the current study.

Another characteristic of the frequency response could be seen by rearranging Equation 11,

$$R(jw) = \frac{1}{\frac{1}{G(jw)} - H'(jw)}. \tag{12}$$

At low frequencies, the denominator converges to $-H'(jw)$. As the frequency increases, the magnitude of $1/G(jw)$ increase, while the magnitude of $H'(jw)$ decreases. There could exist a frequency where the denominator is minimized, which is the natural frequency or the resonant frequency of the system. Such a resonance behavior is clearly observed in Figure 4, at which the reactor is most unstable. It should be noted that the resonant behavior does not indicate instability.

In general, smaller gain at the resonant frequency and larger bandwidth of the resonant peak are indicators of more stable systems [94]. Lastly, it is noted that in Figure 4(b) as well as in Figure 5(b), a dip is observed around 0.23 rad/s, which corresponds to the out-of-core circulation time and the delayed neutrons [60].

In Figure 5, the frequency response for ^{233}U fuel is shown, which possesses similar shapes to the frequency response for ^{235}U fuel. Once again, good agreement is found between the simulation and the experiment. The reactor's gain is generally increased for ^{233}U fuel compared with ^{235}U fuel, indicating it is less stable. Moreover, the dip near 0.23 rad/s is once again observed and is more prominent than that with ^{235}U fuel.

(a) 0 MW

(b) 8 MW
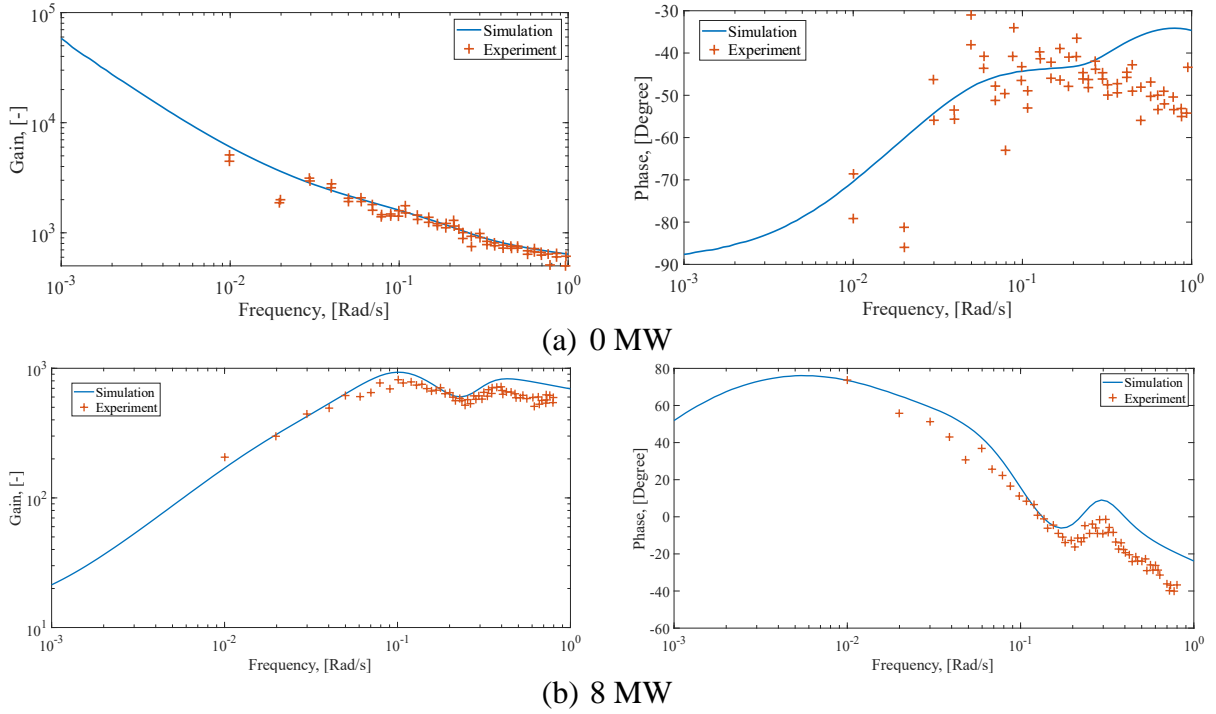
Figure 5. Comparison of the power-to-reactivity frequency response from simulations and experiments with ^{233}U fuel [33, 34].

In Figure 6, the core outlet temperature to power frequency responses from the simulation and the experiment are presented. It is observed that the frequency response directly using the core outlet temperatures deviates from the experimental data, especially at higher frequencies. The same problem is noted in the report by Steffy [34] that the dynamic model used during MSRE could not capture the result. The larger deviation at higher frequencies suggests that the source of disagreement comes from the temperature measurement itself. Thermocouples were used during MSRE for temperature measurement, which have characteristic response times. The response time mainly comes from thermal inertia and the heat transfer conditions in the measurement system. A heuristic transfer function between the thermocouple measurement and the surrounding flow temperature is derived from the one-dimensional heat conduction equation in the Appendix as,

$$M(jw) = \frac{T_m(jw)}{T_\infty(jw)} = \left[\cosh\left(\sqrt{\frac{jw}{\alpha_{th}}} L \right) - \frac{k}{h} \sqrt{\frac{jw}{\alpha_{th}}} \sinh\left(\sqrt{\frac{jw}{\alpha_{th}}} L \right) \right]^{-1}, \qquad (13)$$

where h is the heat transfer coefficient between the thermal couple wall and the fuel salt, L the characteristic length of the thermal couple, α_{th} is the thermal diffusivity of the thermocouple, and k is the thermal conductivity of the thermocouple. The transfer function could be used to convert the true temperature signal at the core outlet to the measured temperature signal.

The thermocouple sheath material used in the MSRE is Inconel, and the thermocouple is placed in the fuel salt using the so-called "INOR-8" lug [95]. The properties of Inconel 718 are used in Equation 13. The heat transfer coefficient is estimated using the following empirical correlation [96],

$$h = \frac{0.683 D_f Re^{0.466} Pr^{1/3}}{2R_{tc}} \approx 6461.8 \ \text{W/m}^2 \cdot \text{K} . \tag{14}$$

Lastly, the characteristic length used in the transfer function is 25.4 mm, which is only a nominal value used to approximate the thermal inertia of the measurement system. The solid lines in Figure 6 represents the simulations where the thermocouple transfer function is applied. The good agreement between the experimental data and the simulation results is rather remarkable, considering the great simplification made in the derivation of the transfer function.
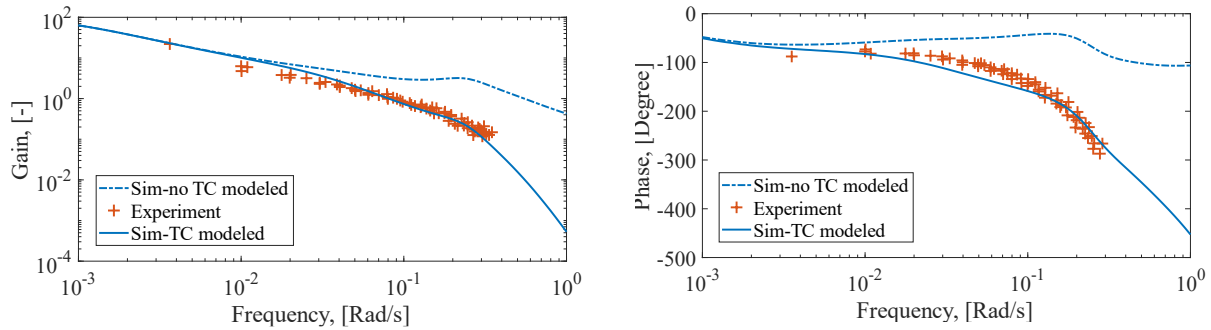
Figure 6. Comparison of the temperature-to-power frequency response from simulations and experiments with ^{233}U fuel [34].

In conclusion, the current coupled model could generally predict the frequency response of the MSRE at zero-power and elevated power levels for both ^{235}U fuel and ^{233}U fuel. There is no significant difference between the two fuel types for the system frequency responses. The good agreement at zero-power serves as a validation of the neutronics model. Moreover, the thermal hydraulics modeling adopted in the study is validated using the temperature-to-power frequency response.

Transient Response

In the previous subsection, the system frequency responses from experiments and simulations are compared. Though the frequency response is a useful representation of the system behavior, it does not have a direct link to the transient response of the reactor. In this subsection, the coupled model is validated against multiple transient experiments in the MSRE.

In the zero-power physics experiment of MSRE, transient responses during pump startup and pump coast-down are measured [38]. At zero-power, feedback effects from thermal and fission product poisoning are absent, and the system response is dictated by the neutronics and hydraulics characteristics of the reactor system.

In the pump startup experiment, the reactor was initially critical while the pumps were idle. At the start of experiment, the pumps were turned on, and salt flow was established. In the pump coast-down experiment, the procedure was reversed. The automatic reactivity control system was enabled during the experiment to maintain the criticality of the reactor. The control rod locations, the pump speeds, and the coolant flowrate were recorded. Unfortunately, the fuel salt flowrate was not available. In the simulation, a hyperbolic tangent function is used to approximate the flowrate in the primary loop.

The simulations of pump transients are compared with the experimental data in Figure 7. Two simulation approaches are applied. In the first approach as depicted by the blue line, the reactor is assumed to stay perfectly at criticality, and the neutron density is not changed. In the second approach as shown by the purple line, a simple proportional controller is introduced as an approximation to the automatic control system employed in the MSRE. A sample frequency of 40

Hz is applied for the neutron density measurement. The proportional parameter is set as -50 pcm percent neutron fraction. The maximum reactivity change rate is limited to 25 pcm per second, matching the control rod specifications in the MSRE [97].

In Figure 7(a), the simulation result of the pump startup transient is shown. Both simulation approaches predict the steady-state reactivity loss accurately, and both failed to predict the initial reactivity peak. The peak observed around 15s is related to the out-of-core circulating time. The simulation with the proportional controller has the fluctuating behavior observed in the experiment, suggesting such fluctuations may be related to the control system in the MSRE. In Figure 7(b), the comparison is shown for the pump coast-down transient. Both simulation approaches capture the general trend of the reactivity change, while the PI controller helps to reproduce the short-period fluctuations.
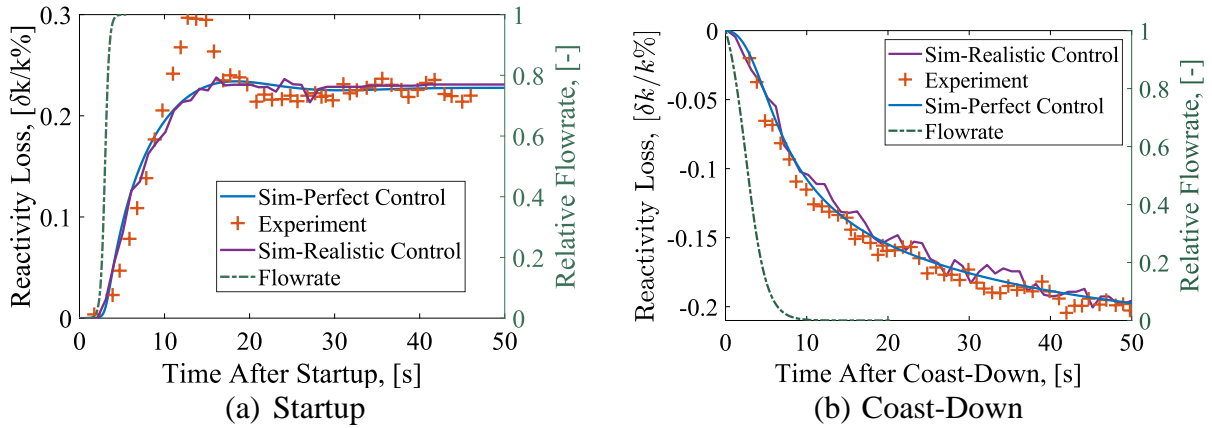

Figure 7. Comparison between the experiment and simulation of the pump transients [38]. The dash-dot line represents the relative flowrate in the primary loop (right axis). The solid lines correspond to the simulation results (left axis).

The fact that both simulation approaches failed to capture the reactivity peak in Figure 7(a) deserves further discussion. In the work by Guo et al. [45] and Shi et al.[53], the simulated

reactivity loss also failed to match the reactivity peak. In these studies, the mPKEs are used with homogeneous DNP distribution in the core as in the current study. On the other hand, in the work by Fischer and Bureš [74], the mPKEs are solved together with 1D DNP transport equations, and the delayed neutron generation term is weighted using steady-state adjunct flux and power profile. Consequently, the long-period fluctuating behavior in the startup transient is observed. Considering the differences in the models, it is argued that the disagreement between the current simulation and the experiment during the startup transient is related to the homogeneous treatment of DNPs inside the core, which smears the sharp reintroduction of delayed neutrons to the core center, where the neutron importance is highest.

In Figure 8, the reactor power following a 19 pcm reactivity insertion at an initial power of 5 MW is shown. The reactor power quickly increases after the reactivity insertion in the first few seconds. Then, as the temperatures of the core increase, the feedback effect comes to offset the added reactivity. The net steady-state result is a slight increase in the reactor power. The simulation generally agrees with the experimental data. In the simulation, the initial power peaking is slightly overestimated, and the slow fluctuations in the power profile is not observed. It should be noted that during the experiments with ^{233}U fuel, notable neutron noise is observed due to the circulating bubbles. The circulating bubbles were considered to be the major source behind the observed fluctuations [34], which is not modeled in the current study.

In conclusion, the current coupled model could generally predict the transient response of the MSRE both at zero-power conditions and operational conditions. Though it is noted that the

mPKEs employed in the current study may require improvements to capture sharp transient behaviors and short-period fluctuations.
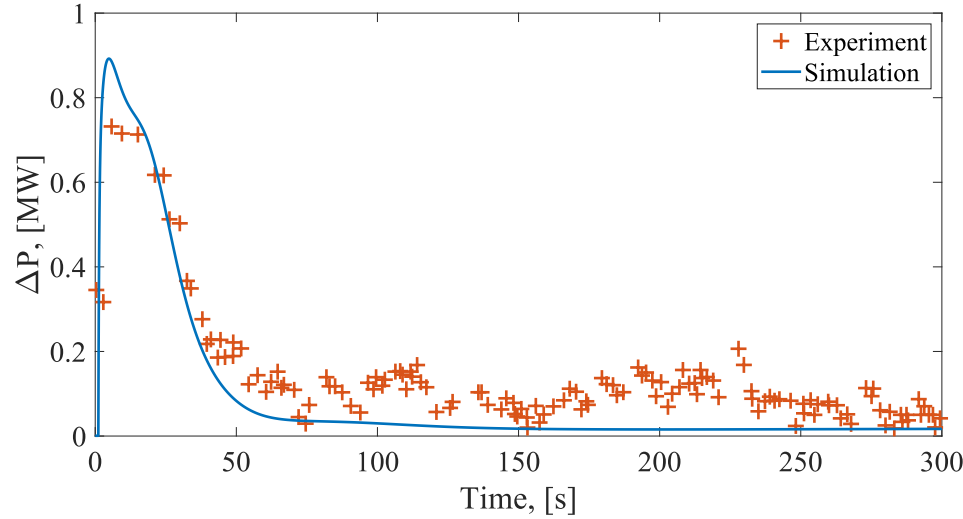

Figure 8. Comparison of the simulated and measured power transients following a 19.0 pcm reactivity insertion at 5 MW with ^{233}U fuel [34].

Model Applications

In the previous sections, the coupled model is validated against the experimental dynamic data from the MSRE. In this section, the model is applied to study the unique dynamic characteristics of the MSRE. Moreover, a sensitivity study of the frequency response to the plant parameters is performed.

Power to Flowrate and Void Frequency Reponses

In the previous section, the power-to-reactivity frequency response of the MSRE is thoroughly investigated, which is of general interest to reactor control and stability analysis. In this section, two other types of frequency responses that are unique to MSRs are investigated.

In Figure 9, the power-to-flowrate frequency responses at different reactor power levels and fuel types are shown. The gain and the flowrate are normalized with operational parameters. The gain in Figure 9 could have two peaks. The first peak corresponds to the resonant frequency or natural frequency of the reactor, which is related to the heat transfer and thermal feedback of the reactor. The second peak is only observed at higher powers, which corresponds to the circulation of DNPs in the primary loop. The peak frequency is at around 0.23 rad/s, corresponding to the loop time of the reactor. It is observed that the gain is larger at lower reactor power, indicating reduced stability.
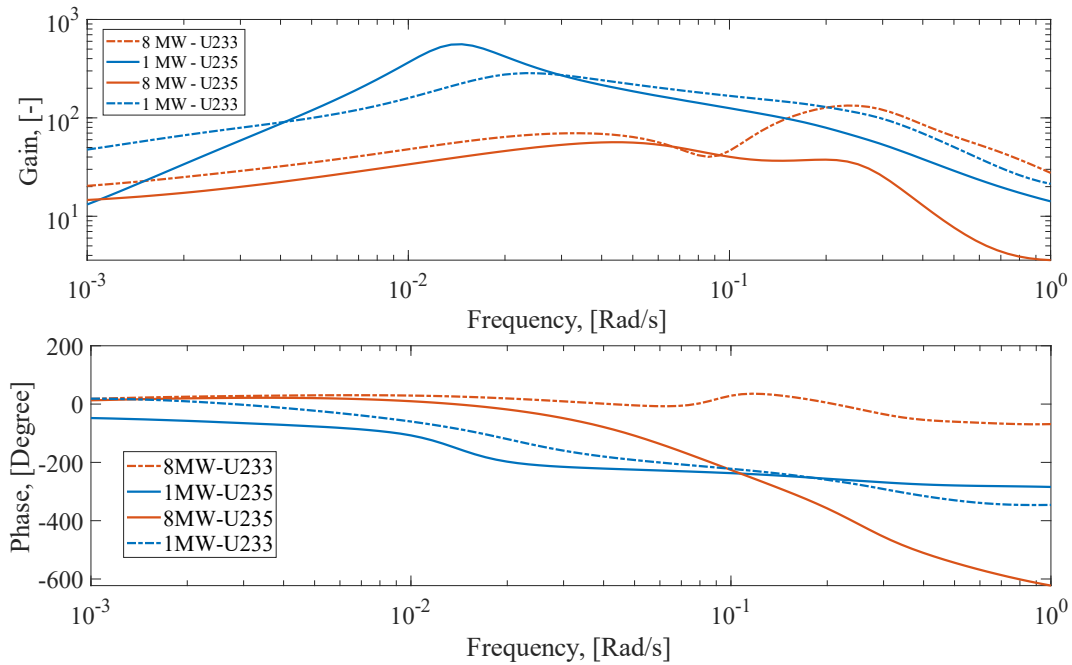

Figure 9. Power-to-flowrate frequency responses of the MSRE.

In Figure 10, the power to core void fraction frequency responses with ^{235}U fuel are plotted at two different powers. The disturbance is initiated at the pump bowl by changing the entrained void fraction. From the results, it is observed that the reactor is relatively insensitive to small

disturbances to the circulating void fraction at 8 MW. Both lines are nearly identical at frequency higher than 0.1 rad/s, corresponding to the timescale of the void feedback effect. The frequency response at lower frequency is also related to the xenon removal and xenon poisoning in the reactor. This effect is comparable to the delayed neutron fraction when the reactor is at power. The reason that such a large reactivity effect is not reflected in the observed frequency response lies in the difference in the characteristic times. The change in xenon poisoning takes place in hours, while the change in effective delayed neutron fraction has a timescale of seconds. The slow reactivity change associated with circulating void fraction may be used for shim control of MSRs.
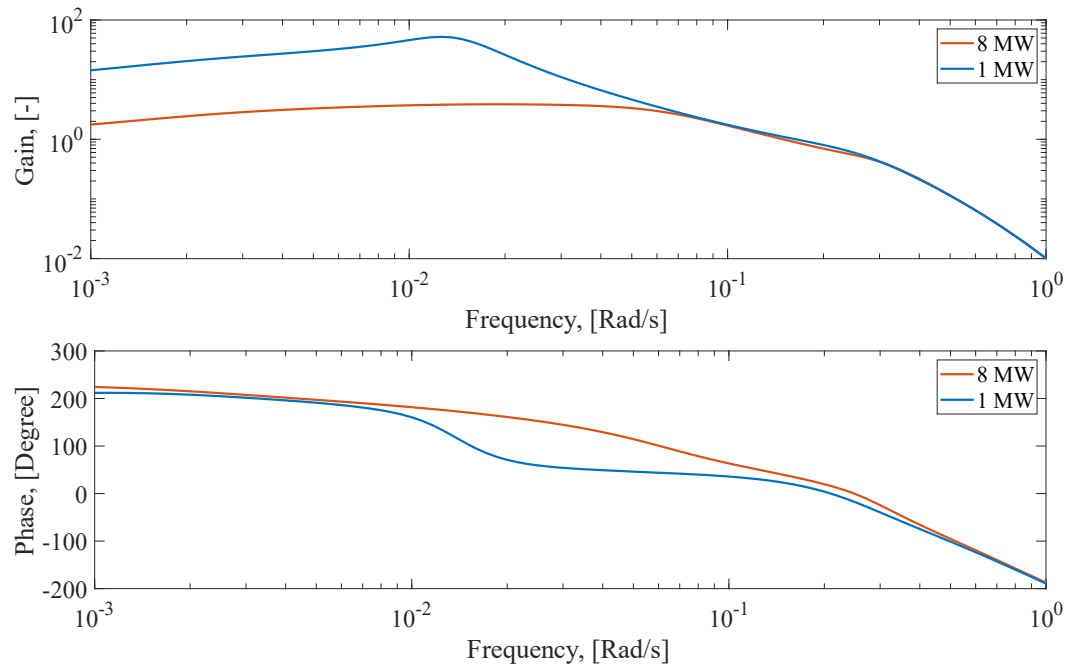

Figure 10. Power to core void fraction frequency response of the MSRE.

Plant Response During Unique Initiating Events

In this subsection, the plant responses during two unique imitating events in MSRs are investigated. The first case is the blockage in the off-gas system. When the off-gas system is

blocked, xenon cannot be removed from the system, and it starts to accumulate in the reactor. This results in a slow reduction in reactivity. The second event is the loss of circulating void fraction due to a change in the condition in the pump bowl. In this event, the reactivity of the reactor first increases due to the removal of core void fraction. However, as xenon removal is hindered by the removal of void fraction, the reactivity will drop in the long term. Simulation of plant responses during these two unique scenarios are made possible by the xenon and void transport capabilities in the coupled model.

In Figure 11, the normalized power, core temperatures, and the xenon poisoning level following a blockage in the off-gas line at different powers are shown. The blockage in the off-gas line prevents the removal of xenon at the pump bowl. It is observed that the reactor power and the core temperatures slowly drop as the xenon poisoning level increases following the initiating event. The reactor power is more stable when the reactor is at higher power, even though the corresponding increases in xenon poisoning is larger. The operating temperature at 1MW is slightly increased to separate the temperature lines. It is shown that the temperature variation is more significant at 8MW to compensate for the higher xenon poisoning level. It is noted that the temperature of fuel increases as the fuel travels through the reactor, while the temperature of the graphite is highest at the third node due to the power density profile. The large temperature variation at higher power suggests that active control is required during this type of event to maintain a sufficient margin over the solidification temperature. On the other hand, limited intervention is needed when the reactor is at lower power.
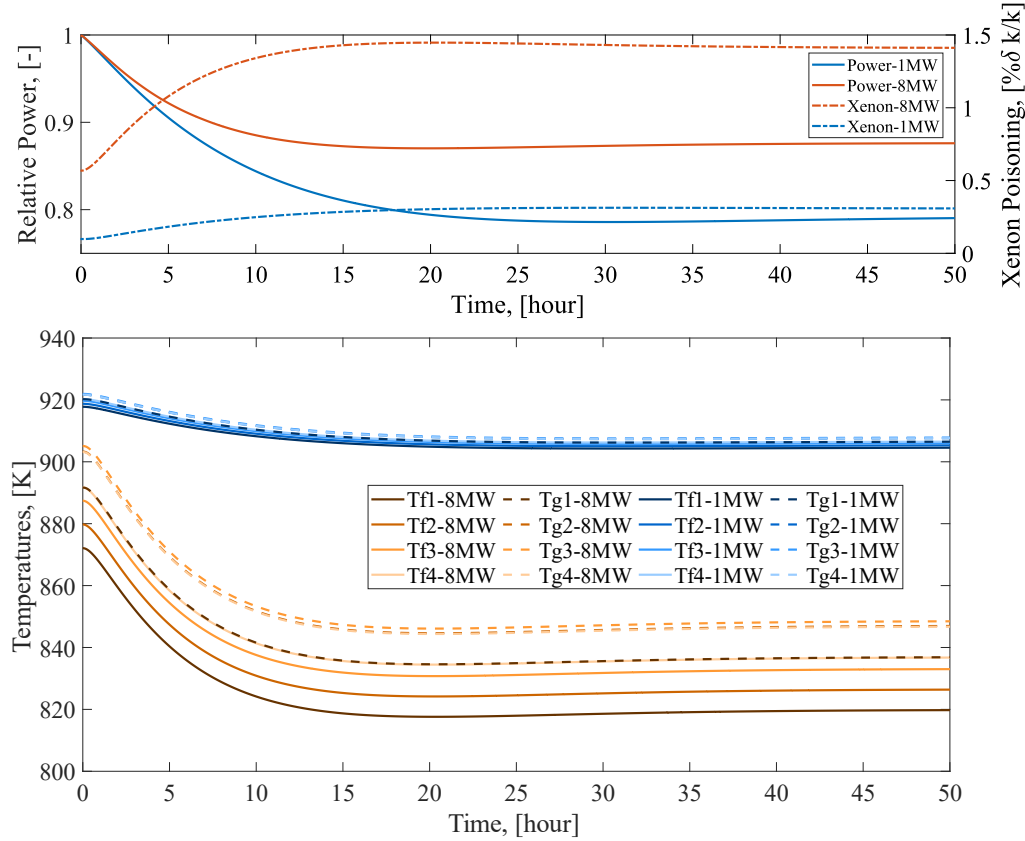
Figure 11. Plant response of the MSRE following a blockage in the off-gas line. In the upper figure, the dash-dot lines correspond to xenon poisoning, while the solid lines correspond to reactor power. In the lower figure, the solid lines correspond to temperatures of the fuel nodes, while the dashed lines correspond to temperatures of the graphite nodes.

In Figure 12 and Figure 13, the plant response following of loss of circulating bubbles at the pump bowl is shown. The response during the first hour is given in Figure 12. The core void fraction lines are almost identical during the event. It is observed that the reactor power rises as the core void fraction decreases. The increase in reactivity due to the loss of core void fraction is countered by the increase in the core temperatures. At higher reactor power, this thermal feedback happens faster, and the resulting power peaking is significantly lower. The xenon poisoning level

only slightly increases in the first hour and does not contribute much to the plant response. In Figure 13, the plant response between the first and fifty hours after the loss of circulating void is shown. The plant response during this period is solely controlled by the increase in xenon inventories due to the absence of circulating bubbles. The plant reaches steady-state in about 30 hours. For reactor at 8MW, the final reactor power is slightly lower than before the event, while the contrary is found for reactor at 1MW. It should be noted that the loss of circulating bubbles does not lead to complete loss of xenon removal, because the spray in the pump bowl is still in operation.
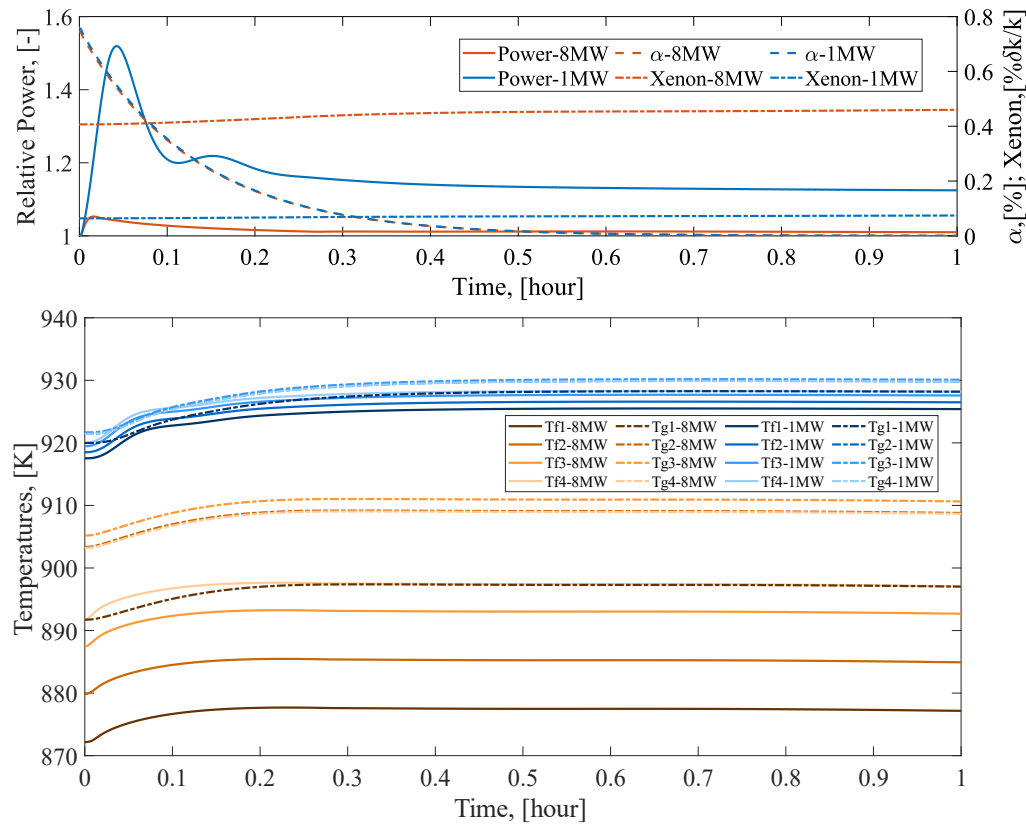
Figure 12. Plant response of the MSRE following the loss of circulating bubbles at the pump bowl in the first hour. In the upper figure, the dash-dot lines correspond to xenon poisoning, the solid

lines correspond to reactor power, and the dashed lines correspond to the core void fraction. In the lower figure, the solid lines correspond to temperatures of the fuel nodes, while the dashed lines correspond to temperatures of the graphite nodes.
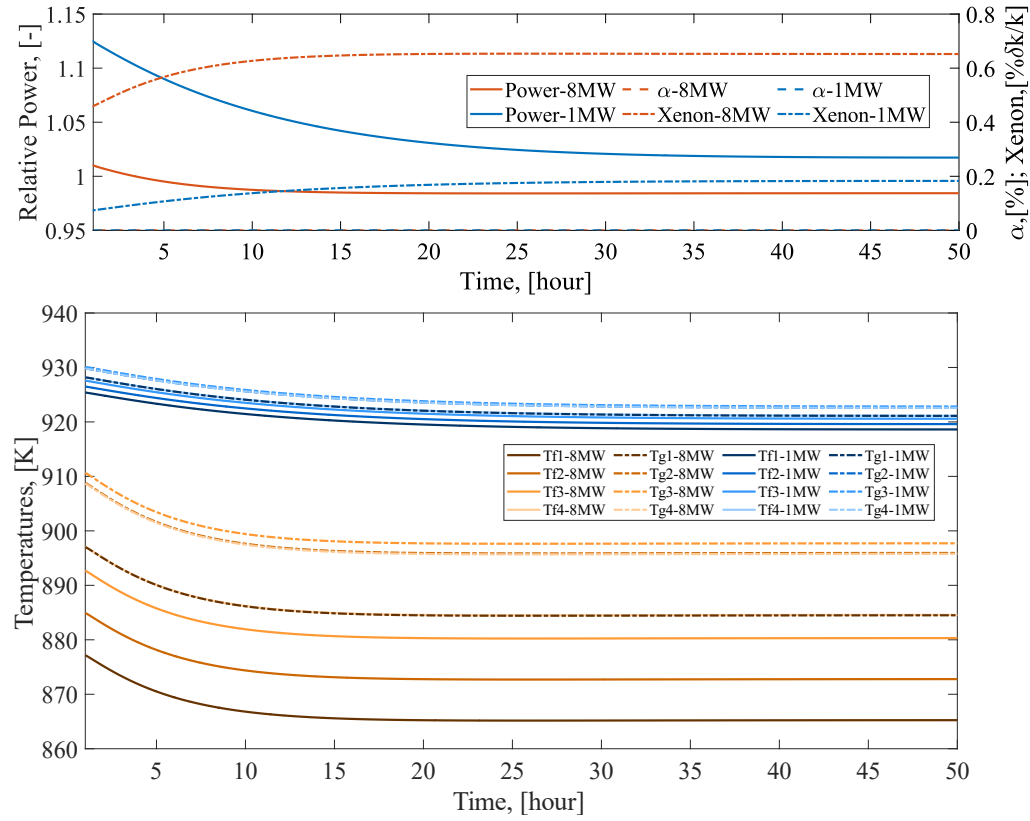

Figure 13. Plant response of the MSRE following the loss of circulating bubbles at the pump bowl from 1h to 50h. In the upper figure, the dash-dot lines correspond to xenon poisoning, the solid lines correspond to reactor power, and the dashed lines correspond to the core void fraction. In the lower figure, the solid lines correspond to temperatures of the fuel nodes, while the dashed lines correspond to temperatures of the graphite nodes.

Frequency Response Sensitivity Study

In this subsection, the sensitivity study of various parameters on the power-to-reactivity frequency response is presneted. Most of the frequency responses included in this subsection are obtained in a different manner from the rest of this work. Instead of using sinusoidal reacitivty signals of different frequencies in multiple simulation cases, a single band-limited white noise signal is applied. The frequency response is obtained by dividing the cross spectral power density by the spectral power density. This approach is analogous to the experimental method adopted in the dynamics testing experiment during the MSRE [33].

The validity of the numerical method adopted in this study is examined in Figure 14. In Figure 14(a), the frequency response obtained using the sinusoidal signals is compared with that obtained using the band-limited white noise signal. It is observed that the results obtained from both method are identical at large frequencies. However, For smaller frequencies, fluctuations are observed in the response obtained using the white noise. The fluctuation is due to insufficient sampling at lower frequencies. In Figure 14(b), the effect of sample time is inllustrated[2]. It is shown that the fluctating behavior is dampened when the sample time is reduced. Though not under the same condition, the white noise used in Figure 14(a) is four times longer than that used in Figure 14(b), and it is observed that the extended sampling time significantly dampens the fluctation at lower frequencies. In Figure 14(c), the effect of DNP nodes is presented. In terms of the frequency

[2] The sample time refers to the maximum time step used in the simulation. Smaller timestep is automatically applied by the solver during quick transient.

responses, no observable difference is found between the uses of 20 nodes and 10 nodes for out-of-core DNP transport.

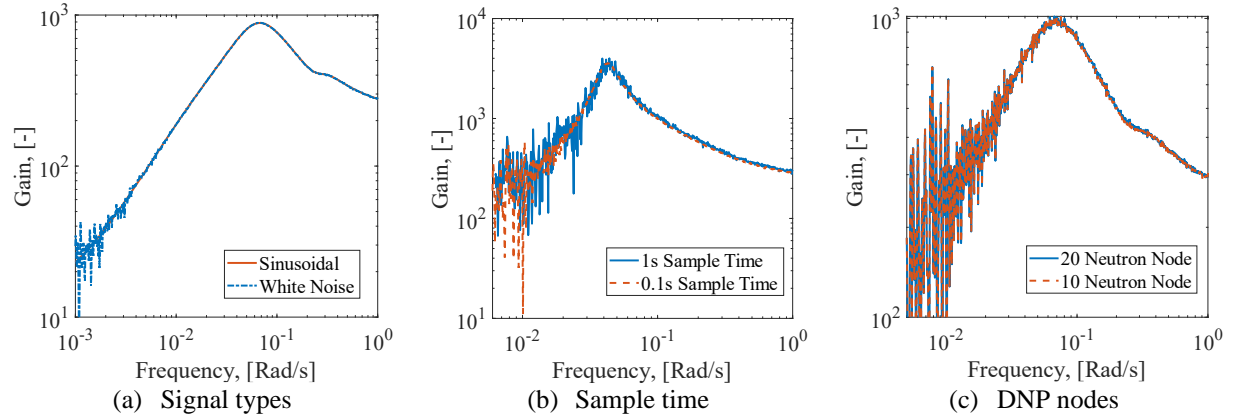(a) Signal types   (b) Sample time   (c) DNP nodes

Figure 14. Effect of sample time and DNP nodes on simulated frequency responses.

In Figure 15, the effect of decay heat generation on the frequency response is presented. The total reactor power in the two cases is maintained at 8 MW. It is shown that the decay heat model slightly shift the resonant peak to lower frequency while overall increasing the power-to-reactivity gain.
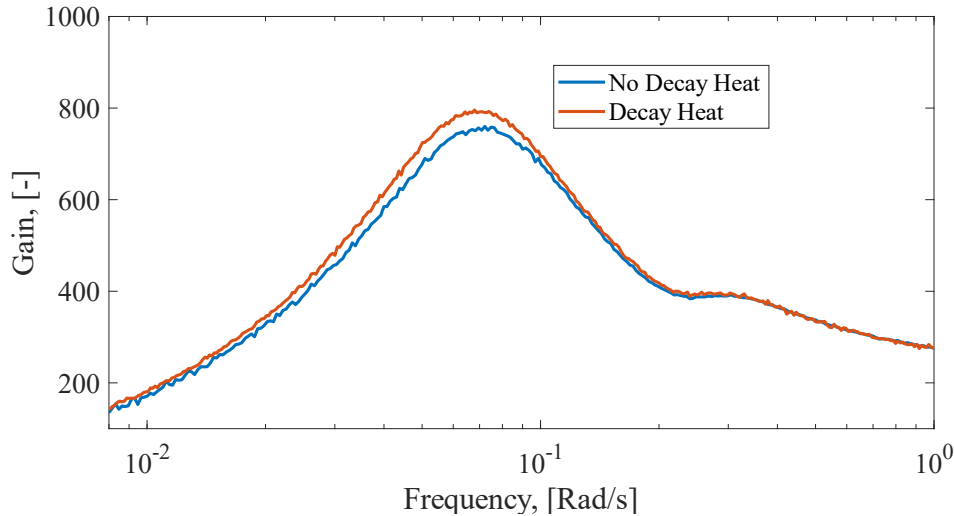

Figure 15. Effect of decay heat generation on the power-to-reactivity frequency response at 8 MW.

The effect of heat capacities on the frequency response is shown in Figure 16. As shown in Figure 16(a) and Figure 16(b), the heat capacities of the fuel salt and graphite have notable influences on the frequency response of the reactor. As most thermal power is deposited into the fuel salt, its heat capacity has a significant impact on the characteristic time of the thermal feedback effect. A higher fuel salt heat capacity shifts the resonance peak to the left and increases its magnitude. On the other hand, though a higher graphite heat capacity also shifts the resonance peak to the lower frequencies, it does not seem to change the height of the resonance peak significantly. Relatively small effect is found from the coolant capacity, as shown in Figure 16(c). The increase of coolant heat capacity reduces the peak height and shifts the peak to higher frequencies. The change in coolant heat capacity increases the overall heat capacity of the reactor, which tends to reinforce the oscillation. On the other hand, it improves the heat transfer at the heat exchanger and the radiator, which should help to suppress oscillation.
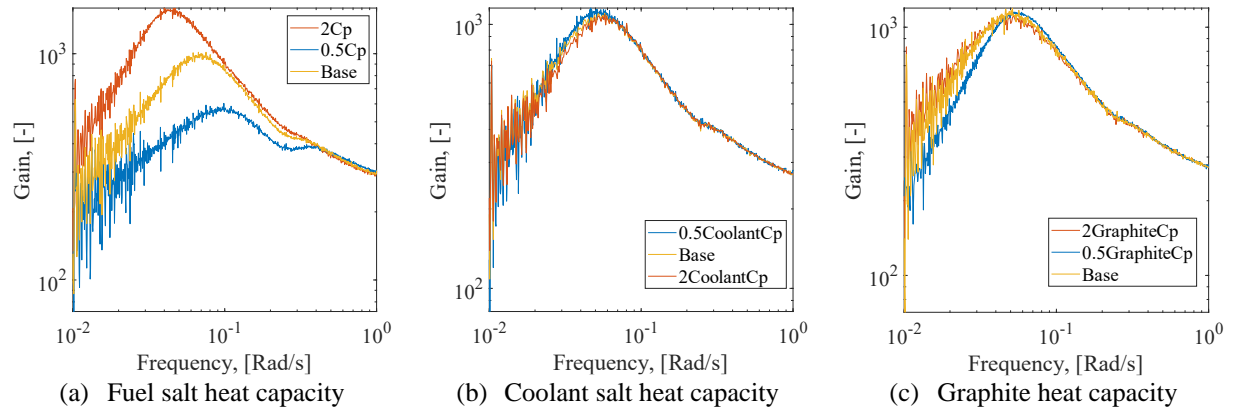

Figure 16. Sensitivity study of different heat capacities on the simulated frequency response.

The effects of different heat transfer coefficients are investigated in Figure 17. It is observed in Figure 17(a) and Figure 17(b) that the salt-graphite heat transfer coefficient and the radiator heat transfer coefficient have negligible effects on the frequency response. The temperature difference

between the graphite and the fuel salt is small, and only a limited fraction of thermal power is deposited into the graphite. Moreover, the heat transfer between the fuel and graphite also involves heat conduction, and the convective heat transfer coefficient turns out not to be the controlling parameter. Similarly, the heat transfer at the MSRE radiator is controlled by the flowrates, temperatures, and heat capacities of the coolant and the air flow, while the heat transfer coefficient is not the controlling parameter. On the other hand, in the study of the PHX, the overall heat transfer coefficient is varied. It is shown that the improvement of heat transfer at the PHX dampens the resonance peak as anticipated.

(a) Salt-graphite convective heat transfer coefficient

(b) Radiator convective heat transfer coefficient
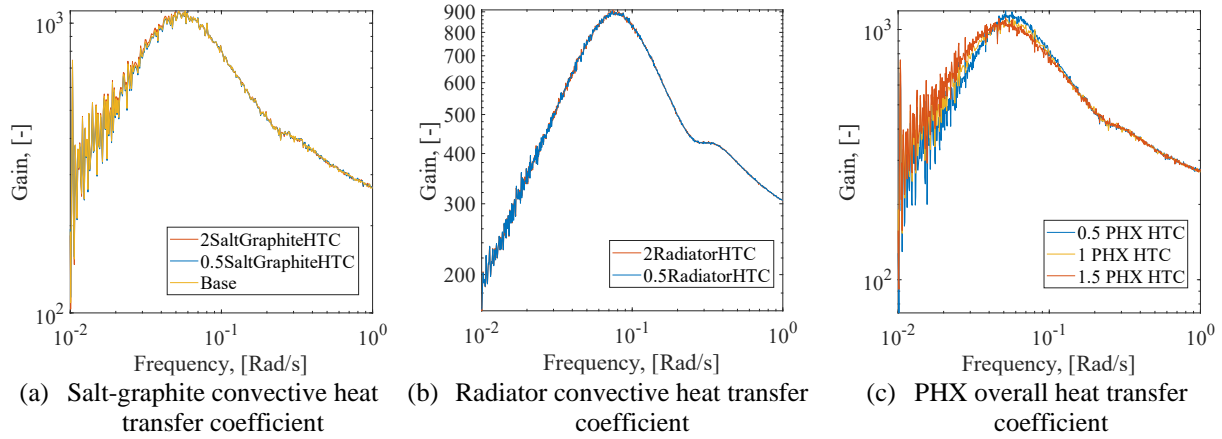
(c) PHX overall heat transfer coefficient

Figure 17. Effect of different heat transfer coefficients on the simulated frequency response.

In Figure 18, the effects of flowrates and the fuel volumes are presented. A reduced fuel salt flowrate leads to a reduction in the frequency response. The dominant effect of reduced fuel flowrate is an increase in the effective delayed neutron fraction, which helps to slow down the transient response of the reactor, corresponding to an overall dampening in the higher frequency region as shown in Figure 18(a). From Figure 18(b), the coolant flowrate has limited effect on the plant responses in the considered range, suggesting that the heat transfer in the secondary loop primarily depends on the air flow at the radiator. In Figure 18(c), the effect of fuel volume in the

reactor core is inspected. It is of practical importance because different values of core fuel volume were reported in the MSRE documents. From the result, it is shown that a higher core fuel volume leads to a lower resonance peak. There are two competing mechanisms at work. On one hand, the increase of core fuel volume leads to a higher effective delayed neutron fraction due to a longer core residence time, which helps to stabilize the reactor. On the other hand, the total fuel heat capacity is increased, which tends to enhance the oscillating behavior.
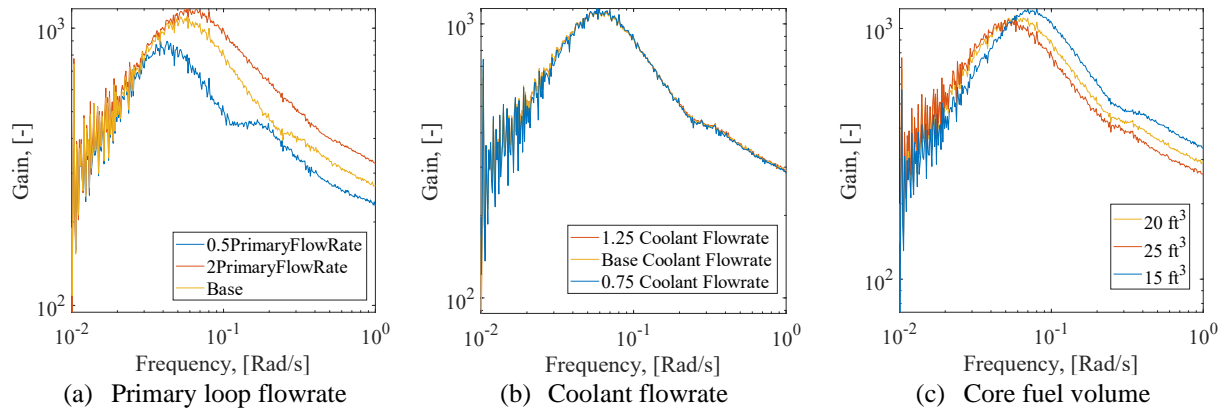

Figure 18. Effect of selected plant parameters on the simulated frequency response.

In Figure 19, the effect of temperature feedback coefficients is shown. It is observed that the increases of the fuel temperature coefficient and the graphite temperature coefficient both reduce the gain at lower frequencies and shift the resonance peak to the right. The fuel temperature coefficient clearly has a stronger impact on the frequency response than the graphite temperature coefficient because of the direct deposition of fission power. It is curious, though, the increase of the graphite temperature coefficient leads to a higher resonance peak, which may be related to the differences in the thermal response times of the graphite and the fuel salt.
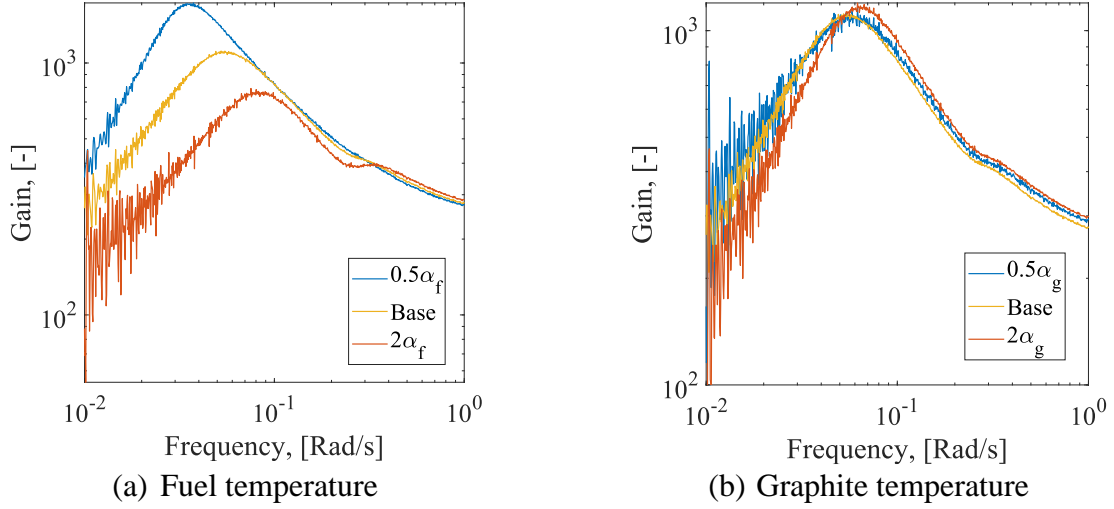
(a) Fuel temperature   (b) Graphite temperature

Figure 19. Effect of temperature feedback coefficients on the simulated frequency response.

Conclusion

In this work, the coupled Simulink model developed in a previous study is extended to study the dynamic behaviors of the MSRE. The model is improved to include nuclear parameters of ^{233}U fuel, the transport of DNPs, decay heat generation, and the secondary loop thermal hydraulics.

The model is validated against the power-to-reactivity frequency responses at different power with ^{233}U fuel and ^{235}U fuel. The zero-power frequency responses serve as a validation of the neutronics model, while the frequency response at power is used to validate the coupled model. The thermal-hydraulics modeling in the current work is also separated validated using the temperature-to-power frequency response of the reactor. In addition to the frequency domain, the model is validated using the reactor transient response during reactivity insertion, pump startup and pump coast-down experiments. Good agreements are found for all conditions except for the pump startup transient. It is argued that the disagreement in the latter case is related to the treatment of DNP transport inside the core.

After the validation, the coupled model is applied to study the unique dynamic characteristics of the MSRE. The power-to-flowrate and power-to-void frequency responses of the MSRE are simulated. It is shown that the MSRE has a smooth power-to-void frequency responses, which may be utilized for reactor shim control. In addition, the plant responses during the unique initiating events of off-gas system blockage and loss of circulating void are simulated. It is shown that the slow reactivity changes related to xenon poisoning during these events do not threaten the reactor's stability and safety. However, the immediate reactivity change during loss-of-void event could cause a notable power peaking at low operational powers. Lastly, a sensitivity study of various plant parameters and the numerical schemes is included.

Declaration of Competing Interest

The authors declare that they have no known competing financial interests or personal relationships that could have appeared to influence the work reported in this paper.

Code Availability

The model is available at https://github.com/jiaqic2014/MSRE_Dynamics-Xenon.

Reference

[1] C.-F. Schleussner, J. Rogelj, M. Schaeffer, T. Lissner, R. Licker, E.M. Fischer, R. Knutti, A. Levermann, K. Frieler, W. Hare, Science and policy characteristics of the Paris Agreement temperature goal, Nature Climate Change 6(9) (2016) 827-835. https://doi.org/10.1038/nclimate3096.
[2] A. Asuega, B.J. Limb, J.C. Quinn, Techno-economic analysis of advanced small modular nuclear reactors, Applied Energy 334 (2023) 120669. https://doi.org/10.1016/j.apenergy.2023.120669.
[3] S. Hong, C.J.A. Bradshaw, B.W. Brook, Global zero-carbon energy pathways using viable mixes of nuclear and renewables, Applied Energy 143 (2015) 451-459. https://doi.org/10.1016/j.apenergy.2015.01.006.

[4] B. Mignacca, G. Locatelli, Economics and finance of molten salt reactors, Progress in Nuclear Energy 129 (2020) 103503. https://doi.org/10.1016/j.pnucene.2020.103503.

[5] M. Lin, M.-S. Cheng, Z.-M. Dai, Feasibility of an innovative long-life molten chloride-cooled reactor, Nuclear Science and Techniques 31(4) (2020) 33. https://doi.org/10.1007/s41365-020-0751-7.

[6] R. Roper, M. Harkema, P. Sabharwall, C. Riddle, B. Chisholm, B. Day, P. Marotta, Molten salt for advanced energy applications: A review, Annals of Nuclear Energy 169 (2022) 108924. https://doi.org/10.1016/j.anucene.2021.108924.

[7] R.C. Robertson, Conceptual design study of a single-fluid Molten-Salt Breeder Reactor, 1971. ORNL-4541.

[8] J.R. Engel, Experience with the Molten-Salt Reactor Experiment, Nuclear Applications and Technology 8(2) (1970) 118-136. https://doi.org/10.13182/NT8-2-118.

[9] C. Wulandari, A. Waris, S. Permana, S. Pramuditya, Evaluating the JEFF 3.1, ENDF/B-VII.0, JENDL 3.3, and JENDL 4.0 nuclear data libraries for a small 100 MWe molten salt reactor with plutonium fuel, Nuclear Science and Techniques 33(12) (2022) 165. https://doi.org/10.1007/s41365-022-01141-8.

[10] X.-C. Zhao, R. Yan, G.-F. Zhu, Y.-F. Liu, J. Guo, X.-Z. Cai, Y. Zou, Plutonium utilization in a small modular molten-salt reactor based on a batch fuel reprocessing scheme, Nuclear Science and Techniques 35(4) (2024) 68. https://doi.org/10.1007/s41365-024-01428-y.

[11] J. Chen, C.S. Brooks, Design and cost-benefit analysis of the xenon removal system for the molten salt demonstration reactor, Annals of Nuclear Energy 207 (2024) 110705. https://doi.org/10.1016/j.anucene.2024.110705.

[12] V. Mishra, E. Branger, S. Grape, Z. Elter, S. Mirmiran, Material attractiveness of irradiated fuel salts from the Seaborg Compact Molten Salt Reactor, Nuclear Engineering and Technology (2024). https://doi.org/10.1016/j.net.2024.04.045.

[13] G.-A. Wen, J.-H. Wu, C.-Y. Zou, X.-Z. Cai, J.-G. Chen, M. Bao, Preliminarysafety analysis for a heavy water-moderated molten salt reactor, Nuclear Science and Techniques 35(6) (2024) 106. https://doi.org/10.1007/s41365-024-01476-4.

[14] Y.-P. Zhang, Y.-W. Ma, J.-H. Wu, J.-G. Chen, X.-Z. Cai, Preliminary analysis of fuel cycle performance for a small modular heavy water-moderated thorium molten salt reactor, Nuclear Science and Techniques 31(11) (2020) 108. https://doi.org/10.1007/s41365-020-00823-5.

[15] M. Rosenthal, P. Kasten, R. Briggs, Molten-salt reactors—history, status, and potential, Nuclear Applications and Technology 8(2) (1970) 107-117. https://doi.org/10.13182/NT70-A28619.

[16] I.A.E. Agency, Non-baseload operation in nuclear power plants: load following and frequency control modes of flexible operation, 2018. No. NP-T-3.23.

[17] G. Chen, M. Li, Y. Zou, H. Xu, Analysis of load-following operation characteristics of liquid fuel molten salt reactor, Progress in Nuclear Energy 150 (2022) 104308. https://doi.org/10.1016/j.pnucene.2022.104308.

[18] E.M. Duchnowski, R.F. Kile, K. Bott, L.L. Snead, J.R. Trelewicz, N.R. Brown, Pre-conceptual high temperature gas-cooled microreactor design utilizing two-phase composite moderators. Part I: Microreactor design and reactor performance, Progress in Nuclear Energy 149 (2022) 104257. https://doi.org/10.1016/j.pnucene.2022.104258.

[19] J.J. DiNunno, F.D. Anderson, R.E. Baker, R.L. Waterfield, Calculation of distance factors for power and test reactor sites, 1962. TID-14844.

[20] J.R. Engel, R.C. Steffy, Xenon behavior in the Molten Salt Reactor Experiment, 1971. ORNL-TM-3464.

[21] S. Shahbazi, D. Grabaskas, S. Thomas, N. Andrews, A. Clark, D. Luxat, M. Higgins, M. Smith, Survey and assessment of computational capabilities for advanced (non-LWR) reactor mechanistic source term analysis, 2020. ANL/NSE-20/39.

[22] D.J. Diamond, N.R. Brown, R. Denning, S. Bajorek, G. Tartal, Phenomena important in modeling and simulation of molten salt reactors, 2018. BNL-114869-2018-IR.

[23] U.S.N.R. Commission, NRC non-light water reactor (non-LWR) vision and strategy, Volume 1–Computer code suite for non-LWR plant systems analysis, 2020. ML20030A176.

[24] U.S.N.R. Commission, NRC non-light water reactor (non-LWR) vision and strategy, Volume 3–Computer code development plans for severe accident progression, source term, and consequence analysis, 2020. ML20030A178.

[25] D. Wooten, J.J. Powers, A review of molten salt reactor kinetics models, Nuclear Science and Engineering 191(3) (2018) 203-230. https://doi.org/10.1080/00295639.2018.1480182.

[26] A. Rykhlevskii, J.W. Bae, K.D. Huff, Modeling and simulation of online reprocessing in the thorium-fueled molten salt breeder reactor, Annals of Nuclear Energy 128 (2019) 366-379. https://doi.org/10.1016/j.anuce.2019.01.030.

[27] X.-C. Zhao, Y. Zou, R. Yan, X.-Z. Cai, Analysis of burnup performance and temperature coefficient for a small modular molten-salt reactor started with plutonium, Nuclear Science and Techniques 34(1) (2023) 17. https://doi.org/10.1007/s41365-022-01155-2.

[28] T.W. Kerlin, S.J. Ball, R.C. Steffy, Theoretical dynamics analysis of the Molten-Salt Reactor Experiment, Nuclear Technology 10(2) (1971) 118-132. https://doi.org/10.13182/NT71-A30920.

[29] D. Zhang, S. Qiu, G. Su, Development of a safety analysis code for molten salt reactors, Nuclear Engineering and Design 239(12) (2009) 2778-2785. https://doi.org/10.1016/j.nucengdes.2009.08.020.

[30] S. Dulla, P. Ravetto, M.M. Rostagno, Neutron kinetics of fluid–fuel systems by the quasi-static method, Annals of Nuclear Energy 31(15) (2004) 1709-1733. https://doi.org/10.1016/j.anucene.2004.05.004.

[31] E. Compere, S. Kirslis, E. Bohlmann, F. Blankenship, W. Grimes, Fission product behavior in the Molten Salt Reactor Experiment, 1975. ORNL-4865.

[32] J. Chen, C.S. Brooks, Modeling of transient and steady state xenon behavior in the Molten Salt Reactor Experiment, Annals of Nuclear Energy (2024). https://doi.org/10.1016/j.anucene.2024.110525.

[33] T. Kerlin, S. Ball, Experimental dynamic analysis of the Molten-Salt Reactor Experiment, 1966. ORNL-TM-1647.

[34] R. Steffy Jr, Experimental dynamic analysis of MSRE with 233 U fuel, 1970. ORNL-TM-2997.

[35] T.W. Kerlin, S.J. Ball, R.C. Steffy, M.R. Buckner, Experiences with Dynamic Testing Methods at the Molten-Salt Reactor Experiment, Nuclear Technology 10(2) (1971) 103-117. https://doi.org/10.13182/NT71-A30919.

[36] J. Krepel, U. Grundmann, U. Rohde, F.-P. Weiss, DYN1D-MSR dynamics code for molten salt reactors, Annals of Nuclear Energy 32(17) (2005) 1799-1824. https://doi.org/10.1016/j.anucene.2005.07.007.

[37] J. Křepel, U. Rohde, U. Grundmann, F.-P. Weiss, DYN3D-MSR spatial dynamics code for molten salt reactors, Annals of Nuclear Energy 34(6) (2007) 449-462. https://doi.org/10.1016/j.anucene.2006.12.011.

[38] B.E. Prince, S.J. Ball, J.R. Engel, P.N. Haubenreich, T.W. Kerlin, Zero-power physics experiments on the Molten-Salt Reactor Experiment, 1968. ORNL-4233.

[39] M.W. Rosenthal, R.B. Briggs, P.R. Kasten, Molten-salt reactor program semiannual progress report for period ending february 28, 1969, 1969. ORNL-4396.

[40] A. Cammi, V. Di Marcello, L. Luzzi, V. Memoli, M.E. Ricotti, A multi-physics modelling approach to the dynamics of Molten Salt Reactors, Annals of Nuclear Energy 38(6) (2011) 1356-1372. https://doi.org/10.1016/j.anucene.2011.01.037.

[41] A. Cammi, C. Fiorina, C. Guerrieri, L. Luzzi, Dimensional effects in the modelling of MSR dynamics: Moving on from simplified schemes of analysis to a multi-physics modelling approach, Nuclear Engineering and Design 246 (2012) 12-26. https://doi.org/10.1016/j.nucengdes.2011.08.002.

[42] M. Zanetti, A. Cammi, C. Fiorina, L. Luzzi, A Geometric Multiscale modelling approach to the analysis of MSR plant dynamics, Progress in Nuclear Energy 83 (2015) 82-98. https://doi.org/10.1016/j.pnucene.2015.02.014.

[43] L. He, C.-G. Yu, R.-M. Ji, W. Guo, Y. Dai, X.-Z. Cai, Development of a dynamics model for graphite-moderated channel-type molten salt reactor, Nuclear Science and Techniques 30(1) (2019) 18. https://doi.org/10.1007/s41365-018-0541-7.

[44] R.C. Diniz, A.d.C. Gonçalves, F.S.d.S. da Rosa, Neutron point kinetics model with precursors' shape function update for molten salt reactor, Nuclear Engineering and Design 360 (2020) 110466. https://doi.org/https://doi.org/10.1016/j.nucengdes.2019.110466.

[45] Z. Guo, D. Zhang, Y. Xiao, W. Tian, G. Su, S. Qiu, Simulations of unprotected loss of heat sink and combination of events accidents for a molten salt reactor, Annals of Nuclear Energy 53 (2013) 309-319. https://doi.org/10.1016/j.anucene.2012.09.009.

[46] D. Zhang, A. Rineiski, C. Wang, Z. Guo, Y. Xiao, S. Qiu, Development of a kinetic model for safety studies of liquid-fuel reactors, Progress in Nuclear Energy 81 (2015) 104-112. https://doi.org/10.1016/j.pnucene.2015.01.011.

[47] K. Zhuang, L. Cao, Y. Zheng, H. Wu, Studies on the molten salt reactor: code development and neutronics analysis of MSRE-type design, Journal of Nuclear Science and Technology 52(2) (2015) 251-263. https://doi.org/10.1080/00223131.2014.944240.

[48] L. Cao, K. Zhuang, Y. Zheng, T. Hu, H. Wu, Transient analysis for liquid-fuel molten salt reactor based on MOREL2.0 code, International Journal of Energy Research 42(1) (2018) 261-275. https://doi.org/10.1002/er.3828.

[49] B. Zhou, X.-H. Yu, Y. Zou, P. Yang, S.-H. Yu, Y.-F. Liu, X.-Z. Kang, G.-F. Zhu, R. Yan, Study on dynamic characteristics of fission products in 2 MW molten salt reactor, Nuclear Science and Techniques 31(2) (2020) 17. https://doi.org/10.1007/s41365-020-0730-z.

[50] J. Richard, D. Wang, G. Yoder, J. Carbajo, D. Williams, B. Forget, C. Forsberg, Implementation of liquid salt working fluids into TRACE, Proceedings of ICAPP 2014, 2014.

[51] X. He, Validation of the TRACE code for the system dynamic simulations of the molten salt reactor experiment and the preliminary study on the dual fluid molten salt reactor, Technische Universität München, 2016.

[52] T. Hanusek, R.M. Juan, Analysis of the Power and Temperature distribution in molten salt reactors with TRACE. Application to the MSRE, Annals of Nuclear Energy 157 (2021) 108208. https://doi.org/10.1016/j.anucene.2021.108208.

[53] C. Shi, M. Cheng, G. Liu, Development and application of a system analysis code for liquid fueled molten salt reactors based on RELAP5 code, Nuclear Engineering and Design 305 (2016) 378-388. https://doi.org/10.1016/j.nucengdes.2016.05.034.

[54] R. Li, M. Cheng, Z. Dai, Improvement of the delayed neutron precursor transport model in RELAP5 for liquid-fueled molten salt reactor, Nuclear Engineering and Design 394 (2022) 111817. https://doi.org/10.1016/j.nucengdes.2022.111817.

[55] J. Fang, R. Hu, M. Gorman, L. Zou, G. Hu, T. Hua, SAM enhancements and model developments for molten-salt-fueled reactors, 2020. ANL/NSE-20/66.

[56] S.A. Walker, M.E. Tano Retamales, A. Abou Jaoude, Application of NEAMS multiphysics framework for species tracking in molten salt reactors, 2023. INL/RPT-23-74376.

[57] G. Yang, L. Zou, R. Hu, Updated SAM model for the Molten Salt Reactor Experiment (MSRE), 2023. ANL/NSE-23/8.

[58] R. Salko Jr, T. Mui, R. Hu, L. Zou, Implementation of a Gas Transport Model in SAM for Modeling of Molten Salt Reactors, 2023.

[59] G. Yang, M.K. Jaradat, W. Sik Yang, C. Lee, Development of coupled PROTEUS-NODAL and SAM code system for multiphysics analysis of molten salt reactors, Annals of Nuclear Energy 168 (2022) 108889. https://doi.org/10.1016/j.anucene.2021.108889.

[60] V. Singh, A.M. Wheeler, M.R. Lish, O. Chvála, B.R. Upadhyaya, Nonlinear dynamic model of Molten-Salt Reactor Experiment – Validation and operational analysis, Annals of Nuclear Energy 113 (2018) 177-193. https://doi.org/10.1016/j.anucene.2017.10.047.

[61] V. Singh, M.R. Lish, O. Chvála, B.R. Upadhyaya, Dynamics and control of molten-salt breeder reactor, Nuclear Engineering and Technology 49(5) (2017) 887-895. https://doi.org/10.1016/j.net.2017.06.003.

[62] I. Singh, A. Gupta, U. Kannan, Studies on reactivity coefficients of thorium-based fuel (Th-233U)O2 with molten salt (Flibe) cooled pebble, Nuclear Science and Engineering 191(2) (2018) 161-177. https://doi.org/10.1080/00295639.2018.1463745.

[63] V. Singh, Study of the dynamic behavior of molten-salt reactors, University of Tennessee, 2019.

[64] V. Singh, A.M. Wheeler, B.R. Upadhyaya, O. Chvála, M.S. Greenwood, Plant-level dynamic modeling of a commercial-scale molten salt reactor system, Nuclear Engineering and Design 360 (2020) 110457. https://doi.org/10.1016/j.nucengdes.2019.110457.

[65] V. Pathirana, O. Chvala, A.M. Wheeler, Scalable modular dynamic molten salt reactor system model with decay heat, Annals of Nuclear Energy 154 (2021) 108060. https://doi.org/10.1016/j.anucene.2020.108060.

[66] V. Pathirana, O. Chvala, S. Skutnik, Depletion dependency of molten salt reactor dynamics, Annals of Nuclear Energy 168 (2022) 108852. https://doi.org/10.1016/j.anucene.2021.108852.

[67] N. Dunkle, O. Chvala, Effect of xenon removal rate on load following in high power thermal spectrum Molten-Salt Reactors (MSRs), Nuclear Engineering and Design 409 (2023) 112329. https://doi.org/10.1016/j.nucengdes.2023.112329.

[68] N. Dunkle, J. Richardson, V. Pathirana, A. Wheeler, O. Chvala, S.E. Skutnik, NERTHUS thermal spectrum molten salt reactor neutronics and dynamic model, Nuclear Engineering and Design 411 (2023) 112390. https://doi.org/10.1016/j.nucengdes.2023.112390.

[69] T.J. Price, O. Chvala, Z. Taylor, Molten salt reactor xenon analysis: review and decomposition, Journal of Nuclear Engineering and Radiation Science 5(4) (2019). https://doi.org/10.1115/1.4043813.

[70] T.J. Price, O. Chvala, Z. Taylor, Xenon in molten salt reactors: the effects of solubility, circulating particulate, ionization, and the sensitivity of the circulating void fraction, Nuclear Engineering and Technology 52(6) (2020) 1131-1136. https://doi.org/10.1016/j.net.2019.11.026.

[71] T. Price, O. Chvala, G. Bereznai, A dynamic model of xenon behavior in the Molten Salt Reactor Experiment, Annals of Nuclear Energy 144 (2020) 107535. https://doi.org/10.1016/j.anucene.2020.107535.

[72] M.S. Greenwood, B.R. Betzler, A.L. Qualls, J. Yoo, C. Rabiti, Demonstration of the Advanced Dynamic System Modeling Tool TRANSFORM in a molten salt reactor application via a model of the Molten Salt Demonstration Reactor, Nuclear Technology 206(3) (2020) 478-504. https://doi.org/10.1080/00295450.2019.1627124.

[73] V. Pathirana, S.E. Creasman, O. Chvála, S. Skutnik, Molten salt reactor system dynamics in simulink and modelica, a code to code comparison, Nuclear Engineering and Design 413 (2023) 112484. https://doi.org/10.1016/j.nucengdes.2023.112484.

[74] L. Fischer, L. Bureš, Application of Modelica/TRANSFORM to system modeling of the molten salt reactor experiment, Nuclear Engineering and Design 416 (2024) 112768. https://doi.org/10.1016/j.nucengdes.2023.112768.

[75] J.-L. Huang, G.-B. Jia, L.-F. Han, W.-Q. Liu, L. Huang, Z.-H. Yang, Dynamic simulation analysis of molten salt reactor-coupled air–steam combined cycle power generation system, Nuclear Science and Techniques 35(2) (2024) 30. https://doi.org/10.1007/s41365-024-01394-5.

[76] J. Chen, GitHub repository for the coupled MSRE model. https://github.com/jiaqic2014/MSRE_Dynamics-Xenon, 2024.

[77] R.E. Thoma, Chemical aspects of MSRE operation, 1970. ORNL-4658.

[78] S. Cantor, Density and viscosity of several molten fluoride mixtures, 1973. ORNL-TM-4308.

[79] W. Powers, S. Cohen, N. Greene, Physical properties of molten reactor fuels and coolants, Nuclear Science and Engineering 17(2) (1963) 200-211.

[80] M.W. Rosenthal, P.N. Haubenreich, F.B. Briggs, Development status of molten-salt breeder reactors, 1972. ORNL-4812.

[81] R.C. Robertson, MSRE design and operations report. Part I. Description of reactor design, 1965. ORNL-TM-728.

[82] P.N. Haubenreich, J.R. Engel, B.E. Prince, H.C. Claiborne, MSRE design and operations report. Part iii. Nuclear analysis, 1964. ORNL-TM-730.

[83] S. Cantor, J.W. Cooke, A.S. Dworkin, G.D. Robbins, R.E. Thoma, G.M. Watson, Physical properties of molten-salt reactor fuel, coolant, and flush salts, 1968. ORNL-TM-2316.

[84] D.M. Tartakovsky, M. Dentz, Diffusion in porous media: phenomena and mechanisms, Transport in Porous Media 130(1) (2019) 105-127. https://doi.org/10.1007/s11242-019-01262-6.

[85] J. Engel, P. Haubenreich, A. Houtzeel, Spray, mist, bubbles, and foam in the Molten Salt Reactor Experiment, 1970. ORNL-TM-3027.

[86] S.J. Ball, T.W. Kerlin, Stability analysis of the Molten-Salt Reactor Experiment, 1965. ORNL-TM-1070.

[87] J. Steffy, R C, P.J. Wood, Theoretical dynamic analysis of the MSRE with 233U fuel, 1969. ORNL-TM-2571.

[88] S. Dulla, E.H. Mund, P. Ravetto, The quasi-static method revisited, Progress in Nuclear Energy 50(8) (2008) 908-920. https://doi.org/10.1016/j.pnucene.2008.04.009.

[89] J. Lewins, Nuclear reactor kinetics and control, Elsevier, 2013.

[90] D.N. Fry, R.C. Kryter, J.C. Robinson, Measurement of helium void fraction in the MSRE fuel salt using neutron noise analysis, 1968. ORNL-TM-2315.

[91] A. Cammi, V. Di Marcello, C. Guerrieri, L. Luzzi, Transfer function modeling of zero-power dynamics of circulating fuel reactors, Journal of Engineering for Gas Turbines and Power 133(5) (2010). https://doi.org/10.1115/1.4002880.

[92] C. Guerrieri, A. Cammi, L. Luzzi, An approach to the MSR dynamics and stability analysis, Progress in Nuclear Energy 67 (2013) 56-73. https://doi.org/10.1016/j.pnucene.2013.03.020.

[93] B.J. Henderson, G.L. Ragan, Transfer functions for circulating-fuel reactors, 1967. LA-3734.

[94] R.C.D.R.H. Bishop, Modern control systems, 2011.

[95] R.L. Moore, MSRE design and operations report. Part IIB. Nuclear and process instrumentation, 1972. ORNL-TM-729(Pt.2B).

[96] T.L. Bergman, Fundamentals of heat and mass transfer, John Wiley & Sons, 2011.

[97] J.R. Tallackson, MSRE design and operations report. Part IIA. Nuclear and process instrumentation, 1968. ORNL-TM-729(Pt.2A).

[98] X.-D. Zuo, M.-S. Cheng, Y.-Q. Dai, K.-C. Yu, Z.-M. Dai, Flow field effect of delayed neutron precursors in liquid-fueled molten salt reactors, Nuclear Science and Techniques 33(8) (2022) 96. https://doi.org/10.1007/s41365-022-01084-0.

Appendix: Thermocouple Transfer Function

The derivation starts from the one-dimensional heat conduction equation,

$$\frac{\partial T(t,x)}{\partial t} = \alpha_{th} \frac{\partial^2 T}{\partial x^2}. \tag{A1}$$

The measurement point locates at $x = 0$, while the boundary locates at $x = L$. The boundary conditions are,

$$\left.\frac{\partial T}{\partial x}\right|_{x=0} = 0, \quad \left[k\left.\frac{\partial T}{\partial x}\right|_{x=L} + h\big(T(t,L) - T_\infty(t)\big)\right] = 0. \tag{A2}$$

Performing Laplace transform on both Equation A1 and Equation A2, the following equations are obtained in the frequency domain,

$$\frac{\partial^2 \tilde{T}}{\partial x^2} - \frac{s}{\alpha_{th}}\tilde{T} = 0, \tag{A3}$$

$$\left.\frac{\partial \tilde{T}}{\partial x}\right|_{x=0} = 0, \quad \left[k\left.\frac{\partial \tilde{T}}{\partial x}\right|_{x=L} + h\left(\tilde{T}(L) - \tilde{T}_\infty(s)\right)\right] = 0. \tag{A4}$$

Equation A3 has the common solution when considering the boundary condition at $x = 0$,

$$\tilde{T} = \tilde{C}(s)\cosh\left(\sqrt{\frac{s}{\alpha_{th}}}\,x\right). \tag{A5}$$

Next, Equation A5 is plugged into the boundary condition at $x = L$ to yield,

$$-k\tilde{C}\sqrt{\frac{s}{\alpha_{th}}}\sinh\left(\sqrt{\frac{s}{\alpha_{th}}}\,L\right) + h\tilde{C}\cosh\left(\sqrt{\frac{s}{\alpha_{th}}}\,L\right) = h\tilde{T}_\infty(s). \tag{A6}$$

Now we rearrange Equation A6, and note that $\tilde{T}(s,0) = \tilde{C}(s)$, which is the temperature measurement in the frequency domain, thus we have,

$$\widetilde{M}(s) = \frac{\tilde{C}}{\tilde{T}_\infty} = \left[\cosh\left(\sqrt{\frac{s}{\alpha_{th}}}L\right) - \frac{k}{h}\sqrt{\frac{s}{\alpha_{th}}}\sinh\left(\sqrt{\frac{s}{\alpha_{th}}}L\right) \right]^{-1} , \qquad (A7)$$

Replacing s with jw, and the transfer function between the measurement temperature and the surrounding temperature is obtained.